

1

Revision 3

2 **Grain-scale zircon Hf isotope heterogeneity inherited from sediment-**
3 **metasomatized mantle: Geochemical and Nd-Hf-Pb-O isotopic constrains on**
4 **Early Cretaceous intrusions in central Lhasa Terrane, Tibetan Plateau**

5 Ming-Jian Li^{1,2}, Yun-Chuan Zeng^{1*}, Massimo Tiepolo², Federico Farina², Ji-Feng Xu¹, Feng
6 Huang¹, Xi-Jun Liu³, Qin Chen⁴, Yuan Ma⁵,

7

8 1 State Key Laboratory of Geological Processes and Mineral Resources, School of Earth Science
9 and Resources, China University of Geosciences, Beijing 100083, China

10 2 Dipartimento di Scienze della Terra “A. Desio”, Università degli Studi di Milano, Via Botticelli
11 23, Milano 20133, Italy

12 3 Guangxi Key Laboratory of Hidden Metallic Ore Deposits Exploration, College of Earth
13 Sciences, Guilin University of Technology, Guilin 541004, China

14 4 The Second Geological Exploration Institute of China Metallurgical Geology Bureau, Fuzhou
15 350108, China

16 5 China Railway Design Corporation, Tianjin 300142, China

17 *Corresponding author: Yun-Chuan Zeng

18 Address: No. 825 Yifu Building, China University of Geosciences, Beijing, No. 29, Xueyuan
19 Road, Haidian District, Beijing, 100083

20 Tel: 86-13001135869 and email: zengyc@cugb.edu.cn

21

22

Abstract

23 Clarifying the mechanism of recycling of pre-existing continental crustal materials into the
24 source of mantle-derived magma is a challenging effort that can be of great value to improve our
25 understanding of mantle processes and continental crust growth. This study presents an integrated

26 investigation of whole-rock and mineral geochemical and Nd-Hf-O-Pb isotopic data for dolerites
27 and diorites intruded in the central Lhasa Terrane of Tibetan Plateau at ca. 120 Ma (zircon U-Pb
28 ages). These intrusions have similar distributions of trace elements that are characterized by
29 depletion in Nb-Ta relative to Th, Ba and U, and moderately negative whole-rock $\epsilon_{Nd}(t)$ (-5.0 to -
30 1.7) values. Magmatic zircon shows dramatically variable $\epsilon_{Hf}(t)$ values (from -5.0 to +13.7 in the
31 same rock, including up to 12 epsilon unit variability in single grains). On the other hand, the
32 zircon $\delta^{18}O$ values are relatively uniform (+6.0‰ to +7.7‰). The constant $^{208}Pb/^{206}Pb$ values of
33 clinopyroxene crystallized at ca. 500–900 MPa suggest no contamination with lower continental
34 crust. The lack of covariation between Hf and O isotopes from the same grains, and the lack of
35 relationship between Hf isotopes and trace elements (e.g., Hf, Th/U and Yb/Gd) in the magmatic
36 zircons, together with the absence of ancient zircon xenocrysts, implies limited upper crustal
37 contamination. In combination with high whole-rock Th/La (>0.29) ratios, we interpret the zircon
38 Hf isotope heterogeneity as inherited from a depleted asthenospheric mantle with the addition of
39 1–4 % Hf from isotopically heterogeneous sediments. Our study therefore emphasizes the need for
40 caution when using complex Hf isotopic zonation in zircon as an argument for intracrustal
41 hybridization of two end-member magmas derived from distinct reservoirs. In addition, the high
42 Zr/Y ratios and no negative Zr-Hf anomalies of the Aruo intrusions imply a high surface
43 temperature of the downgoing slab that was able to fully dissolve zircons in the subducted
44 sediments. This requires a special geodynamic condition that was most likely related to the
45 steepening of flatly subducted Neo-Tethyan lithosphere at ca. 120 Ma according to a synthesis of
46 regional tectonic-magmatic-sedimentary records.

47

48 **Keywords:** Zircon Hf heterogeneity, sedimentary recycling, mantle metasomatism, magma
49 mixing, Lhasa Terrane

50

51

Introduction

52 Recycling of pre-existing continental crustal materials in magmatic arcs is a fundamental
53 process controlling the chemistry and evolution of the continental crust. The involvement of a
54 crustal component in arc-related magmas has been widely recognized and is typically manifested
55 by the enriched radiogenic (e.g., Sr-Nd-Hf) isotope composition. This can be achieved in two

56 profoundly different ways, either in the mantle through the addition of subducted material (mostly
57 sediments), or in the crust by assimilation and contamination of mantle-derived precursors (e.g.,
58 [Hawkesworth et al. 1979](#); [Gasparon et al. 1994](#)). Distinguishing the two opposing mechanisms is
59 not easy unless unequivocal evidence, for example sediment-derived magmas intruding the
60 peridotite mantle wedge, is preserved (e.g., [Zeng et al., 2016](#); [Spencer et al., 2017](#)), but is crucial
61 to determine the rates and volumes of continental growth and recycling.

62 Zircon is an ideal mineral to trace source complexity and evolution of the parent magma, as it
63 is chemically stable and has the potential to provide information on crystallization age (U–Pb),
64 radiogenic (Hf) and stable (O) isotopes, as well as on melt compositions ([Valley et al., 2005](#);
65 [Kemp et al., 2007](#); [Grimes et al., 2015](#)). Studies based on combined U–Pb, Hf and O isotopes
66 measured within single zircon grains have significantly advanced our capacity to understand the
67 role of mantle and sediment (or mature continent crust) components in the petrogenesis of
68 granitoid, as well as to enhance our insight into the timing of continental crust growth (e.g., [Kemp
69 et al. 2007](#)). Substantial variation of zircon $\epsilon_{\text{Hf}}(t)$ values has been recognized in granitoid
70 worldwide and is commonly interpreted as evidence of mixing of magma derived from
71 isotopically different reservoirs ([Kemp et al., 2007](#); [Farina et al., 2018](#)), non-equilibrium melting
72 of individual crustal sources ([Tang et al., 2014](#)) or due to local processes involving zircon
73 dissolution and recrystallization ([Villaros et al., 2012](#), [Farina et al., 2014](#), [Finch et al., 2021](#)).
74 However, subducted sediments may also play a significant role in the Hf budget of arc magmas, as
75 exemplified by the Banda arc where the mafic rocks underwent no or very limited crust
76 contamination but present substantial changes in Hf isotopes ($\epsilon_{\text{Hf}} = -3.8$ to $+12.5$) with only little
77 variation in $\delta^{18}\text{O}$ of $+5.8\text{‰}$ – $+7.5\text{‰}$ ([Nebel et al. 2011](#)). This phenomenon indicates that zircon Hf
78 isotope heterogeneity in granitoids may occur in mafic magmas that are free from any kind of
79 assimilation. However, in comparison with granitoids, large Hf isotopes variations at grain-scale
80 are rather rare in zircon from mafic rocks, probably due to higher crystallization temperature
81 and/or less abundance of zircons in mafic magma system.

82 In this paper, we present zircon U–Pb, Lu–Hf and O isotopic, whole-rock geochemical and
83 Sr–Nd isotopic, and in situ clinopyroxene elemental and Pb isotopic data, for some newly
84 identified Early Cretaceous dolerites and diorites in the Aruo area of central Lhasa Terrane,

85 Tibetan Plateau. The combined datasets lead us to contend that dramatic zircon Hf isotope
86 heterogeneities are not caused by intracrustal mixing of crust- and mantle-derived magma. We
87 argue instead that the isotopic variability is inherited from a depleted asthenospheric mantle
88 metasomatized by 1-4% sediment with heterogeneous Hf isotopes.

89

90

Geological background and sample descriptions

91 The Tibetan Plateau consists of four E-W-trending tectonic units, which from north to south
92 are the Songpan-Ganzi, Qiangtang, Lhasa and Himalaya terranes separated by three main suture
93 zones (Yin and Harrison, 2000). As the leading edge of the India-Asia collision, the Lhasa Terrane
94 is sandwiched between the Bangong-Nujiang suture zone (BNSZ) and the Indus-Yarlung Zangbo
95 suture zone (IYZSZ) (Fig. 1a). The BNSZ represents the remnants of the Meso-Tethys Ocean,
96 which was proposed to have closed in the Late Jurassic or the Early Cretaceous (Zeng et al.,
97 2021a). The Meso-Tethys Ocean slab has subducted northwards beneath the Qiangtang Terrane
98 since Early Jurassic (Li et al., 2014, Li et al., 2020), but it remains a controversy whether this
99 paleo-ocean slab has ever subducted towards south beneath the Lhasa Terrane (e.g., Zeng et al.,
100 2018; Li et al., 2018). The IYZSZ represents the remnants of the Neo-Tethyan lithosphere that
101 started to subduct beneath the Lhasa Terrane at Middle Triassic and closed at Early Paleogene
102 following the suturing of Indian and Asian continents (Kang et al., 2014; Kapp and DeCelles,
103 2019).

104 Based mainly on plentiful zircon ε_{Hf} data from intermediate-felsic igneous rocks and
105 sediment cover, the Lhasa Terrane can be divided into northern, central, and southern parts,
106 separated by the Shiquan River-Nam Tso Mélange Zone and the Luobadui-Milashan Fault,
107 respectively (Fig. 1; Zhu et al., 2011a). The northern Lhasa Terrane is covered by Middle Triassic–
108 Cretaceous sedimentary rocks and contains widespread Early Cretaceous magmatic rocks which
109 predominantly have positive zircon ε_{Hf} values. The magmatic rocks exposed in the central Lhasa
110 terrane are dominantly Early Cretaceous granitoid and volcanic rocks. The zircon ε_{Hf} values of
111 these rocks are rather negative, which, in combination with the Cambrian-Paleozoic sediment
112 cover, likely suggests the presence of ancient basement materials. The southern Lhasa terrane is
113 mainly composed of Jurassic-Paleogene Gangdese batholith and associated volcanic successions
114 (Ji et al., 2009; Kang et al., 2014). The overall positive zircon ε_{Hf} values of the Mesozoic

115 magmatic rocks of this subterranean indicate a juvenile nature of the continental crust, although
116 Precambrian basement has been locally identified in eastern and western parts (Hou et al., 2015).

117 Samples in the present study were collected from the northeast bank of the Kering Lake, ~70
118 km NW of Xainza Town (Fig. 1), which tectonically belongs to the central Lhasa Terrane. In
119 addition to Quaternary deposits, the strata exposed in the study area are mainly composed of
120 Devonian Chaguolama Formation limestone; Permian Xiala Formation limestone, Angjie
121 Formation shale, mudstone and siltstone; and Lower Cretaceous Duoni Formation sandstone,
122 siltstone and mudstone. The dolerites and diorites occur as intrusions with irregular map patterns,
123 with diameters hundreds of meters, which intruded the siltstones of the Lower Permian Angjie
124 Formation (Fig. 1b) in the Early Cretaceous, based on previous K-Ar dating (134 Ma; Wang et al.,
125 2002). In addition, some Early Cretaceous basalts-basaltic andesites are exposed to the south of
126 the Aruo intrusions (Fig. 1b; Kang, 2009).

127 The Aruo dolerites and diorite are medium-fine-grained and are mainly composed of euhedral
128 plagioclase, subhedral to euhedral clinopyroxene and amphibole with accessory minerals such as
129 titanite, zircon, ilmenite, and apatite. In addition, some pyroxene and plagioclase grains have been
130 converted to epidote by post-emplacement alteration (Fig. 2). It is noteworthy that some of the
131 euhedral plagioclase grains are wrapped by clinopyroxene and amphibole (Figs. 2b-2c) suggesting
132 the plagioclase crystallized before clinopyroxenes and amphiboles.

133

134

Analytical methods

Zircon U-Pb, O and Lu-Hf isotope analyses

135
136 Zircons were separated by standard density and magnetic separation techniques and
137 individually selected by hand-picking under a binocular microscope. Zircon oxygen isotope
138 analyses were carried out before U-Pb and Lu-Hf isotope determinations. Zircon oxygen isotopes
139 were measured using the SHRIMP IIe-MC equipped with a Cs ion source at the Beijing SHRIMP
140 Center. During the analysis, a 3 nA beam of Cs⁺ was focused into a spot 20 μm elliptical on the
141 target surface. The detailed analytical procedures were similar to those described by Ickert et al.
142 (2008). The measured oxygen isotopic data were corrected for instrumental mass fractionation
143 using the Qinghu zircon ($\delta^{18}\text{O}_{\text{VSMOW}} = +5.3 \text{ ‰}$) as the external standard (Li et al., 2013). Eleven
144 measurements of the internal standard PengLai zircon grains during the course of this study yield

145 a weighted mean of $\delta^{18}\text{O} = +5.30 \pm 0.19 \text{ ‰}$, which is identical within errors to the reported value
146 of $+5.31 \pm 0.10 \text{ ‰}$ (Li et al., 2010). Measured $^{18}\text{O}/^{16}\text{O}$ is normalized to VSMOW, and then
147 corrected for the instrumental mass fractionation factor (IMF) as follows: $(\delta^{18}\text{O})_{\text{M}} = ((^{18}\text{O}/^{16}\text{O})_{\text{M}} /$
148 $0.0020052 - 1) \times 1000$; $\text{IMF} = (\delta^{18}\text{O})_{\text{M(standard)}} - (\delta^{18}\text{O})_{\text{VSMOW}}$; $\delta^{18}\text{O}_{\text{sample}} = (\delta^{18}\text{O})_{\text{M}} + \text{IMF}$.

149 Zircon U–Pb isotopic analyses were conducted in five analytical sessions by using laser
150 ablation-inductively coupled plasma-mass spectrometry (LA–ICP–MS) at the Guilin University of
151 Technology (GUT). Cathodoluminescence images were used to select the appropriate zircon
152 grains for analysis. Laser sampling was performed using a GeoLasHD LA system. An Agilent
153 7900 ICP-MS instrument was used to acquire ion-signal intensities. A detailed description of the
154 laboratory and sample preparation methods, following the guidelines in
155 <http://www.plasmage.org/recommendations> and recommended in Horstwood et al. (2016) are
156 available as metadata (Table S1). Prior to sample analysis, an additional nitrogen gas flow (4
157 mL/min) was used to improve the instrumental sensitivity. Helium and Ar were the carrier and the
158 make-up gas, respectively, and were mixed via a T-connector before entering the ICP. Following
159 about 20 s period of background analysis, samples were spot ablated for 60 s at a 6 Hz repetition
160 rate with a spot size of 32 μm beam and laser energy of 10 J/cm^2 at the sample surface. Plesovice
161 zircon ($^{206}\text{Pb}/^{238}\text{U}$ age = 337 Ma; Sláma et al., 2008) and NIST 610 were analyzed as U-Pb and
162 trace element external standards, respectively. GJ-1 standard zircon was measured as unknown
163 samples to the quality of monitor trace elements. During the course of this study, the analyzed GJ-
164 1 standard zircon grains yielded a weighted $^{206}\text{Pb}/^{238}\text{U}$ age of $605 \pm 1 \text{ Ma}$ (1σ , $\text{MSWD} = 0.3$, $n =$
165 40 ; Table S2), which is consistent with the recommended U–Pb age in allowed precision
166 ($^{206}\text{Pb}/^{238}\text{U}$ age = $608.5 \pm 0.4 \text{ Ma}$; Jackson et al., 2004). In addition, the trace element
167 concentrations of GJ-1 standard zircon were also consistent with the reference values (Table S3).

168 The Lu–Hf isotopic compositions of dated zircons were determined using an MC–ICP–MS
169 coupled with the laser ablation system at GUT. Analyses were conducted using a beam diameter of
170 44 μm and a laser pulse frequency of 10 Hz. The GJ-1 zircon was used as an external standard to
171 monitor data quality. The ratios of $^{176}\text{Lu}/^{175}\text{Lu} = 0.02655$, $^{172}\text{Yb}/^{176}\text{Yb} = 0.5887$, $\beta\text{Yb} =$
172 $0.8725 \times \beta\text{Hf}$ (βHf and βYb refer to the mass bias of Hf and Yb, respectively) obtained during our
173 analysis were used in the isobaric interference correction, consistent with the reference value (Wu

174 [et al., 2006](#)). The stable $^{178}\text{Hf}/^{177}\text{Hf}$ and $^{180}\text{Hf}/^{177}\text{Hf}$ ratios of GJ-1 zircon grains analyzed in this
175 study were 1.46715 ± 0.00023 and 1.88689 ± 0.00024 (2σ , $n = 48$), respectively, which are within
176 200 ppm of known values based upon atomic masses and abundances as recommended by [Spencer](#)
177 [et al. \(2020\)](#). The $^{176}\text{Hf}/^{177}\text{Hf}$ ratios of GJ-1 zircon grains during the course of this study range
178 from 0.281970 ± 16 to 0.282048 ± 20 with a mean value of 0.282009 ± 0.000016 (2σ ; $n = 48$),
179 consistent with the reference value (0.282015 ± 0.000019 , 2σ ; [Elhlou et al., 2006](#)) within allowed
180 analytical errors.

181

182 **Whole-rock major and trace elements analyses**

183 Major and trace element analyses were conducted using an XRF-1500 X-ray fluorescence
184 analyzer and a double focusing high resolution inductively coupled plasma-mass spectrometer
185 (ICP-MS) at the Institute of Geology and Geophysics, Chinese Academy of Sciences. The loss on
186 ignition (LOI) values were measured firstly. About 2.0 g powdered samples were baked in the
187 muffle furnace for more than 2 hours at 915 °C. Then about 0.6 g baked samples were fluxed with
188 $\text{Li}_2\text{B}_4\text{O}_7$ (6g) at $\sim 1200^\circ\text{C}$ to make homogeneous glass disks for major elements determination.
189 During analysis, the USGS standard reference materials (GSR-1, GSR-2 and GSR-3) were used to
190 monitor the data quality. The analytical precision was better than 5%.

191 For trace elements analysis, 40 mg sample powders were dissolved in Teflon bakery using a
192 hybrid acid (1mL 22 M HF, 0.5mL 8 M HNO_3) at 120 °C. Then the solutions were dried and the
193 residues were dissolved using the hybrid acid (1.5mL 22 M HF, 0.5mL 8 M HNO_3) again and
194 moved in the high-pressure bombs at 200 °C for 5 days. After that, the sample solutions were
195 dried again and dissolved with 2.0 mL 8 M HNO_3 in the bombs at 150 °C for 24 hours. After
196 repeating the previous steps, solutions were transferred into PE bottles with 50 g 1% HNO_3
197 containing 10 ppt In. During the procedure, the USGS standard reference materials (GSR-1, GSR-
198 2, and GSR-3) and two blank samples were taken as the external calibration standards. The
199 analytical precision was better than 10%.

200

201 **Whole-rock Sr-Nd isotope analyses**

202 Powdered samples (~ 100 mg) for Sr and Nd isotopic analyses were dissolved first using a 1:3
203 mixture of HF and HNO_3 for 7 days at 120 °C in PFA beakers. The solutions were evaporated to

204 approximately dry at 120 °C, and the residues were dissolved in 16 M HNO₃ and then
205 evaporated again. Subsequently, the residues were re-dissolved in 1 mL 16 M HNO₃, and insulated
206 at 120 °C for over 4 hours. The solutions were re-evaporated at 120 °C, and the residues were
207 dissolved in 2 mL 2M HNO₃ at 120 °C for over 2 hours, which were centrifuged and prepared to
208 separation of the target elements. Strontium and rare earth elements (REE) were separated using a
209 cationic resin. The REE solutions was then processed through HDEHP resin to obtain purified Nd.
210 Strontium and neodymium isotopes were measured by Neptune Plus multi-collector (MC)–ICP–
211 MS at GUT. The Sr and Nd isotopic data were obtained on MC-ICP-MS and normalized to
212 $^{86}\text{Sr}/^{88}\text{Sr} = 0.1194$ and $^{146}\text{Nd}/^{144}\text{Nd} = 0.7219$, respectively. $^{87}\text{Rb}/^{86}\text{Sr}$ and $^{147}\text{Sm}/^{144}\text{Nd}$ ratios were
213 calculated from abundances of these trace elements measured by ICP-MS. The USGS standard
214 reference materials (BHVO-2, GSR-1, and GSR-3) were used to monitor the data quality. The Sr
215 and Nd isotopes of BHVO-2 ($^{87}\text{Sr}/^{86}\text{Sr} = 0.703542 \pm 6$, $^{143}\text{Nd}/^{144}\text{Nd} = 0.512959 \pm 5$), GSR-1
216 ($^{87}\text{Sr}/^{86}\text{Sr} = 0.738340 \pm 7$, $^{143}\text{Nd}/^{144}\text{Nd} = 0.512217 \pm 6$), and GSR-3 ($^{87}\text{Sr}/^{86}\text{Sr} = 0.704131 \pm 6$,
217 $^{143}\text{Nd}/^{144}\text{Nd} = 0.512892 \pm 5$) are consistent with the reference values (Weis et al., 2006; Bao et al.,
218 2018).

219

220 **In situ elemental and Pb isotopic compositions of minerals**

221 Major element compositions of clinopyroxene and amphibole were determined using a JOEL
222 JXA 8230 electron microprobe at the Shandong Analysis Center of China Metallurgical Geology
223 Bureau. Analytical conditions for the electron microprobe were 15 kV accelerating voltage, 20 nA
224 beam current, 10–20 s counting time and 10 μm electron beam diameter. Natural and synthetic
225 materials were used as standards.

226 Major and trace elements of clinopyroxene were measured by using the LA–ICP–MS at the
227 GUT. Laser ablation was undertaken at a constant energy 10 J/cm² and at 10 Hz with a spot
228 diameter of 46 μm. Trace element concentrations were calibrated by using international standards
229 including NIST 610, BCR-2G, BIR-1G and BHVO-2G. Detailed analytical methods and the
230 operating conditions for the laser ablation system are given by Liu et al. (2008).

231 In situ analysis of Pb isotopes in clinopyroxene used MC-ICP-MS (Thermo Scientific)
232 equipped with a 193 nm laser ablation system (Resonetics) at the Guangzhou Institute of
233 Geochemistry, Chinese Academy of Sciences. An X-skimmer cone and additional nitrogen gas

234 flow (2 mL/min) were used to improve the instrumental sensitivity. Isotope signals were detected
235 with ion counters in the static mode. During the first 28s, the gas blank of the system was
236 monitored. In the following 30s, the signals of laser ablation on clinopyroxene were collected. The
237 analytical procedures were described in detail by [Zhang et al. \(2014\)](#). Repeated analyses of the
238 international basaltic glass BHVO-2G yielded mean values of $^{208}\text{Pb}/^{206}\text{Pb} = 2.054 \pm 0.004$ (2σ ,
239 $n = 9$) and $^{207}\text{Pb}/^{206}\text{Pb} = 0.833 \pm 0.001$ (2σ , $n = 9$), which are consistent with the reported values
240 (2.048 and 0.832, respectively; [Elburg et al., 2005](#); [Zhang et al., 2014](#)).

241

242

Results

243 Analytical results from zircon (O and Lu–Hf isotopes, U–Pb ages, and trace elements), whole
244 rocks (Sr and Sm–Nd isotopes, major and trace elements), and clinopyroxenes (trace elements and
245 Pb isotopes) are listed in [Table S2–S9](#).

Zircon U–Pb ages and trace elements

246
247 Zircons separated from two dolerite samples (18AR-01 and 19AR-03) and one diorite sample
248 (19AR-01) were analyzed for U–Pb isotopes and trace elements ([Tables S2–S3](#)). All zircon grains
249 were colorless and subhedral to euhedral, have variable sizes (~50–300 μm) with length-to-width
250 ratios of 1:1–3:1, display high Th/U ratios (1.4–2.8), and present clear oscillatory or banded
251 zoning in cathodoluminescence images ([Fig. 3](#)).

252 A total of 65 zircons from sample 18AR-01 were analyzed, seven of which did not yield
253 concordant results, probably because of Pb loss, although they have similar $^{206}\text{Pb}/^{238}\text{U}$ ages to
254 those of the other zircons. The remaining 58 spots yielded similar concordant zircon $^{206}\text{Pb}/^{238}\text{U}$
255 ages varying from 125.3 ± 2 to 117.4 ± 2 Ma with a weighted mean of 119.7 ± 0.5 Ma ($\pm 1\sigma$,
256 MSWD = 0.43; [Fig. 4a](#)). Similarly, 107 of 115 analytical spots on zircons from sample 19AR-03
257 yielded concordant zircon $^{206}\text{Pb}/^{238}\text{U}$ ages varying from 124.7 ± 1 to 117.0 ± 3 Ma with a weighted
258 mean of 119.9 ± 0.3 Ma ($\pm 1\sigma$, MSWD = 0.75, [Fig. 4b](#)). Nineteen of twenty-six analytical spots on
259 zircon grains from sample 19AR-01 yielded concordant zircon $^{206}\text{Pb}/^{238}\text{U}$ ages varying from 120.4
260 ± 2 to 117.0 ± 1 Ma with a weighted mean age of 118.6 ± 0.7 Ma ($\pm 1\sigma$, MSWD = 0.72 [Fig. 4c](#)).
261 Our new zircon geochronological data imply that the Aruo diorites and dolerites were coevally
262 formed at ca. 120 Ma instead of 134 Ma as suggested by previous K–Ar dating ([Wang et al., 2002](#)).

263 The chondrite normalized rare earth element (REE) patterns of the analyzed zircon grains are

264 similar and are characterized by positive Ce and negative Eu anomalies, strong depletions in
265 light(L)REE relative to heavy(H)REE (Fig. 4d).

266

267 **Zircon Lu-Hf and O isotopes**

268 The ($^{176}\text{Hf}/^{177}\text{Hf}$)_i of zircons from dolerites (a total of 291 analyses on zircon grains of sample
269 18AR-01 and 19AR-03) exhibit a wide range of 0.282557–0.283084 with corresponding $\epsilon_{\text{Hf}}(t)$
270 values of –5.0 to +13.7 and $T_{\text{DM-Hf}}$ ages (Hf depleted mantle model ages; Griffin et al., 2000) of
271 258–1224 Ma (Fig. 5; Table S4). The $\epsilon_{\text{Hf}}(t)$ heterogeneity is also observed in some individual
272 grains with up to 12 epsilon units in the same individual grain (Figs. 3 and 5). Besides, the $\epsilon_{\text{Hf}}(t)$
273 values vary irregularly. For example, as shown in Fig. 3, low $\epsilon_{\text{Hf}}(t)$ core with high $\epsilon_{\text{Hf}}(t)$ rim, high
274 $\epsilon_{\text{Hf}}(t)$ rim with low $\epsilon_{\text{Hf}}(t)$ core, are both developed. In addition, repeatedly varied $\epsilon_{\text{Hf}}(t)$ values are
275 observed in the same individual grain (Fig. 3c). Thirteen zircon grains from diorite sample (19AR-
276 01) also exhibit heterogeneous ($^{176}\text{Hf}/^{177}\text{Hf}$)_i values of 0.282908–0.283141, with corresponding
277 $\epsilon_{\text{Hf}}(t)$ values of +6.3 to +15.1 and $T_{\text{DM-Hf}}$ ages of 190–768Ma.

278 The zircons of dolerite (sample 19AR-03) have restricted variability in oxygen isotopes with
279 $\delta^{18}\text{O}$ values of +6.0‰ to +7.2‰ (Fig. 3; Table S4) and a mean value of +6.8‰ \pm 0.21‰ ($\pm 2\sigma$; n =
280 42), which are slightly higher than those (+5.3 \pm 0.6‰; 2σ) of igneous zircons in equilibrium with
281 mantle-derived magmas (Valley, 2003).

282

283 **Whole-rock major and trace elements**

284 The petrographic observations (Fig. 2) and moderate LOI values (2.3–3.9 wt. %) suggest that
285 the investigated rocks were altered after emplacement. However, based on the following
286 evidences, we contend post-emplacement alteration played a negligible role in modifying the
287 whole-rock chemical makeup. There is no correlation between LOI and fluid-mobile major
288 elements (e.g., K₂O and Na₂O; not shown). Instead, the two elements are in good correlation with
289 TiO₂ and Al₂O₃ (Fig. S1) that are relatively immobile during alteration (Dilek and Furnes, 2011;
290 Pearce, 2014). In terms of trace elements, all samples display coherent chondrite-normalized REE
291 and primitive mantle-normalized multi-element pattern (with the notable exception of Sr),
292 suggesting that these elements were relatively immobile during metamorphism. We further test the
293 mobility of target elements by their relationships with the most fluid-immobile elements, i.e., Nb

294 (e.g., Kurtz et al., 2000; Hastie et al., 2007). For example, the good correlations between Nb and
295 elements such as Y, La, Eu, Ba, and Ce, this suggests that these elements survived alteration,
296 whereas Sr underwent significant change.

297 Sixteen representative Aruo intrusions were analyzed for whole-rock major and trace
298 elements (Table S5). In the following descriptions and diagrams, the contents of all major
299 elements were recalculated on a normalized anhydrous basis. Consistent with the petrography, the
300 majority of the samples plot in the gabbro, gabbroic diorite and diorite fields on the SiO₂-
301 Na₂O + K₂O diagram (Fig. 6a). With increasing SiO₂ content, the major oxides show roughly
302 negative (e.g., MgO, Fe₂O₃^T, TiO₂, and CaO) or positive (Al₂O₃, K₂O) relationship (Fig. 7). On
303 the SiO₂ vs FeO^T/MgO plot, the Aruo intrusions show an evolutionary trend from low-K tholeiitic
304 to calc-alkaline (Fig. 6b).

305 All samples show low contents of compatible elements with (Ni = 2.26–21.9 ppm, Cr = 8.22–
306 76.2 ppm). The primitive mantle-normalized trace-element distributions exhibit enrichment in
307 large ion lithophile elements (LILE; e.g., Rb, U), depletion in high field strength elements (e. g.,
308 Nb, Ta), and no negative Zr and Hf anomalies (Fig. 8). The Aruo intrusions show moderate
309 enrichment in LREE relative to HREE on the chondrite-normalized patterns ((La/Yb)_N = 3.74–
310 4.97) with negligible Eu anomalies ($\delta\text{Eu} = 0.85\text{--}1.02$, $\delta\text{Eu} = \text{Eu}_N / (\text{Sm}_N \times \text{Gd}_N)^{1/2}$).

311

312 **Whole-rock Sr-Nd isotopes**

313 Ten samples were analyzed for Sr–Nd isotopes (Table S6). The initial Sr–Nd isotopes were
314 corrected to 120 Ma based on zircon U–Pb dating. The age-corrected (⁸⁷Sr/⁸⁶Sr)_i values of the
315 Aruo intrusions are variable (0.7064 to 0.7105), probably because the original Sr contents and
316 isotopic signature of these rocks have been disturbed by post-emplacement alteration as suggested
317 above. In comparison, the (¹⁴³Nd/¹⁴⁴Nd)_i values are relatively uniform (0.512239 to 0.512409)
318 with corresponding to ε_{Nd}(t) values of -1.5 and -4.8 and T_{DM-Nd} of 1295–2017 Ma (Fig. 9).

319

320 **Mineral chemistry**

321 This and our previous studies (Zeng et al., 2021a, b) demonstrate that the major elements of
322 clinopyroxene obtained by the two independent techniques (LA-ICP-MS and EPMA) are identical

323 within analytical errors; therefore, we refer to both in the following descriptions.

324 The clinopyroxenes in dolerites are augitic ($\text{Wo}_{36-47}\text{En}_{37-43}\text{Fs}_{15-24}$; Fig. 10) and exhibit
325 moderately varied CaO, MgO, and FeO contents (17.14–22.28 wt. %, 12.71–15.27 wt. % and
326 8.95–14.18 wt. % respectively; Table S7). Clinopyroxenes from the diorites are similar to those in
327 the dolerites and show strong compositional variations (CaO = 16.09–21.73 wt. %, MgO = 11.50–
328 16.95 wt. %, and FeO = 6.81–16.33 wt. %).

329 The amphiboles from one dolerite sample (19AR-05) are magnesio-hornblende and
330 tschermakitic pargasite, and have major element contents as follows: SiO_2 (40.02–44.25 wt.%),
331 CaO (10.39–12.33 wt.%), MgO (11.48–12.55 wt.%), TiO_2 (2.55–3.74 wt.%), FeO (14.66–16.58
332 wt.%), and Al_2O_3 (9.09–10.76 wt.%) and contain minor amounts of Na_2O (1.95–2.72 wt.%) and
333 K_2O (0.58–0.78 wt.%; Table S8).

334 The trace element composition of clinopyroxenes in dolerite and diorite are similar in
335 general. The chondrite-normalized REE pattern is characterized by depletion in LREE relative to
336 HREE ($(\text{La}/\text{Sm})_N = 0.23\text{--}0.86$; $(\text{La}/\text{Yb})_N = 0.33\text{--}1.21$, where the average is average 0.51). The
337 primitive mantle-normalized trace element patterns show Nb, Ta, Zr, Hf, Sr and Eu depletion
338 relative to the neighboring elements and variable Ba, Th and U enrichments (Fig. 10). The Sr
339 values are uniform or slightly decreasing with decreasing Mg#, which, together with the negligible
340 positive Eu anomalies and the petrographic observations, implies that clinopyroxene crystallized
341 simultaneous with and/or after plagioclase (Fig. 11).

342 The initial Pb isotopes of Clinopyroxene are corrected to 120 Ma following the methods of
343 Zhang et al. (2014). Clinopyroxene from two dolerite samples (19AR-04 and 19AR-05) exhibit
344 relatively homogeneous Pb isotopic compositions with $(^{208}\text{Pb}/^{206}\text{Pb})_i$ and $(^{207}\text{Pb}/^{206}\text{Pb})_i$ ratios
345 varying from 2.102 to 2.145 and from 0.844 to 0.863, respectively (Figs. 11c–11d; Table S9).

346

347 Discussion

348 Physical condition during crystallization

349 The chemistry of clinopyroxene is sensitive to melt temperature and pressure, but most
350 thermometers and barometers require an initial assumption of pressure and temperature,
351 respectively. The clinopyroxene-melt thermobarometer of Putirka et al. (2003) can simultaneously
352 estimate the crystallization pressure and temperature if the equilibrated liquid (e.g., whole-rock,

353 glass, or matrix) composition is known. However, the premise of using this thermobarometer is
354 that the clinopyroxene should be chemically in equilibrium with the melt (usually represented by
355 the glass, matrix, or whole-rock composition). The equilibrium can be tested by the Fe–Mg
356 exchange coefficient [$K_D(\text{Fe–Mg})^{\text{clinopyroxene–melt}}$] between the clinopyroxene and the assumed melt,
357 which should be 0.28 ± 0.16 ($\pm 2\sigma$; [Putirka, 2008](#)) if they are chemically equilibrated. As shown in
358 Fig. 10d, the clinopyroxene and whole-rock compositions are equilibrated, providing us access to
359 adequately use the clinopyroxene–melt thermobarometer. The clinopyroxenes of dolerite
360 crystallized under temperatures of 1149–1197 °C (average temperature is 1162 °C) and pressures
361 of 590–935 MPa (corresponding to a continental depth of 18 to 29 km). The clinopyroxenes of
362 diorite crystallized at lower temperatures of 999–1094 °C (average temperature is 1050 °C) and
363 pressures of 49–515 MPa (corresponding to a continental depth of 2 to 17 km; [Table S7](#)).

364 Amphibole compositions provide us another independent access to infer the physicochemical
365 conditions of melt crystallization. By using the methods of [Ridolfi et al. \(2010\)](#), the temperatures,
366 H₂O contents and pressures for magma in equilibrium with amphibole grains in the Aruo
367 intrusions, are 863–937 °C, 4.2–5.9 wt. %, and 190–280 MPa (corresponding to a continental
368 depth of 9 to 13 km), respectively ([Table S8](#)). Because the Aruo intrusions are not cumulate rocks,
369 the physicochemical estimations based on the mineral geothermobarometer are indicative of the
370 pressure, temperature, and water content occurring in the magma during the crystallization of the
371 target minerals. Thus, these results suggest that the parental magmas of the Aruo intrusions were
372 H₂O-rich and underwent a polybaric evolution with the crystallization of clinopyroxene at depth
373 (18–29 km) and that of amphibole at shallower levels (9–13 km).

374

375 **Nature of the source**

376 **Magma differentiation**

377 The MgO (3.7–5.9 wt. %), Mg# (42.1–47.2), Cr (8.22–71.0 ppm) and Ni (2.26–12.5 ppm)
378 values of the Aruo intrusions are much lower than those of primary mantle-derived melts
379 (Mg# = 68–76, Cr > 300 ppm, Ni > 200ppm; [Roeder and Emslie, 1970](#)), indicating a considerable
380 degree of differentiation of their parent magma. Fractional crystallization and assimilation of pre-
381 existing continental crust are two end-member mechanisms responsible for the observed chemical

382 variations in the Aruo intrusions. The heterogeneous zircon Hf isotopes plausibly suggest that
383 intracrustal assimilation or mixing might have played an important role during magmatic
384 evolution. However, as demonstrated by MELTS simulation and simple binary mixing modeling
385 of magma evolution, crustal assimilation fails to explain the initial increase in Al₂O₃
386 concentrations followed by the Al₂O₃ decrease and SiO₂ increase (Fig. 7b). Moreover, a
387 significant crustal assimilation is inconsistent with the variations in Th/Nb, Th/La and Nd isotopes
388 (Fig. 9). Therefore, we suggest that the chemical diversity of the Aruo intrusions are mainly
389 controlled by crystallization differentiation, and we will test the reason(s) of the zircon Hf isotope
390 heterogeneity in detail later. Simulation results and the negative correlations of SiO₂ with MgO,
391 Fe₂O₃^T, TiO₂, and CaO (Fig. 7) indicate that olivine, clinopyroxene, and Fe-Ti oxides were the
392 main fractionated phases (Fig. 2). The negligible to slightly positive Eu anomalies ($\delta\text{Eu} = 0.87\text{--}$
393 1.02 ; Fig. 8; Table S5), and the increasing in Al₂O₃ contents with increasing SiO₂ contents until 60
394 wt. % (Fig. 7b) suggest minimal or no fractionation of plagioclases in the mafic to intermediate
395 rocks.

396

397 **Origin of the zircon Hf isotopes heterogeneity**

398 There are several alternative ways to account for the zircon Hf isotope heterogeneity of the
399 Aruo rocks. First, we need to exclude that the Hf variability is related to analytical issues. An
400 inaccurate interference correction can lead to miscalculation of ¹⁷⁶Hf/¹⁷⁷Hf values, and analytical
401 inaccuracies are amplified proportionally to the ¹⁷⁶Yb/¹⁷⁷Hf of the analyzed crystals. For example,
402 a 0.1% inaccurate correction will lead to a miscalculation of ¹⁷⁶Hf/¹⁷⁷Hf values by about $\sim 2 \epsilon_{\text{HF}}$
403 units for zircon crystals with ¹⁷⁶Yb/¹⁷⁷Hf as low as 0.05 (Fisher et al., 2014; Farina et al., 2014).
404 Moreover, an inaccurate interference correction should give rise to a positive correlation between
405 ¹⁷⁶Yb/¹⁷⁷Hf and ¹⁷⁶Hf/¹⁷⁷Hf (Fisher et al. 2014). The great majority of zircons in the Aruo rocks
406 have ¹⁷⁶Yb/¹⁷⁷Hf ranging between 0.02 and 0.05, together with no positive correlation between
407 ¹⁷⁶Hf/¹⁷⁷Hf and ¹⁷⁶Yb/¹⁷⁷Hf (Fig. S2a), suggesting the Hf isotopic variability described reflects a
408 natural process rather being an analytical artifact.

409 The $\epsilon_{\text{HF}}(t)$ variability in zircon thus argues for the involvement of isotopically different
410 components. The Lhasa lithospheric mantle has suffered multiple stages of metasomatism via
411 oceanic or continental subduction since the Proterozoic (e.g., Yin and Harrison, 2000; Zhu et al.,

412 [2011a; Hu et al., 2018; etc](#)), which should have extremely enriched the Hf isotopic signature (Fig.
413 5a; Zhu et al., 2012; Hu et al., 2018). Besides, the central Lhasa Terrane is underlain by an ancient
414 basement as demonstrated by the local exposure of high-grade metamorphic rocks and the
415 negative zircon $\epsilon_{\text{Hf}}(t)$ values of the Late Triassic-Jurassic granitoids ([Zhu et al., 2011b; Fig. 5a](#)).
416 Therefore, the depleted end-member can only be the asthenospheric mantle, which gains support
417 from the fact that the highest ϵ_{Hf} values in the Aruo zircons are similar to those observed in the
418 regional Jurassic MORB-type rocks ($\epsilon_{\text{Hf}}(t) = +12.8$ and $+17.7$; [Tang et al., 2020](#)).

419 These two components (enriched and depleted end-members) are both participating in the
420 petrogenesis of the Aruo intrusion and four hypotheses can be formulated to account for the origin
421 of these rocks: (1) the enriched components come from the lithospheric mantle; (2) the enriched
422 component comes from the assimilation of an ancient basement (lower continental crust) with low
423 $\epsilon_{\text{Hf}}(t)$ and $\epsilon_{\text{Nd}}(t)$ but equilibrated with the mantle for oxygen; (3) the addition of an upper crustal
424 component at shallow level via assimilation of the country rocks; (4) partial melting of the
425 asthenosphere (depleted component) metasomatized by a crustal (sediment) component coming
426 from the oceanic slab. Below we test the four hypotheses in detail.

427 Firstly, the constant $^{208}\text{Pb}/^{206}\text{Pb}$ values of the Aruo clinopyroxene are inconsistent with
428 mixing between magmas derived from the asthenospheric and lithospheric mantle. This view is
429 further supported by the binary mixing model of trace element ratios (in particular Th/La; [Fig. 9](#)).
430 The basement of the Lhasa Terrane is directly sampled by recently discovered Triassic gneiss
431 exposed in the Rendui area ([Fig. 1a; Zhou, 2017](#)), yet, the Sr-Nd-Pb isotopic signature of this
432 gneiss remains unknown. The Early Cretaceous Cuoqen metaluminous dacites are interpreted as
433 melts of the Lhasa basement ([Huang et al., 2017](#)), as supported by their similar zircon ϵ_{Hf} values
434 with the metamorphic zircons of Rendui gneiss that are much higher than the S-type granites in
435 central Lhasa Terrane. It is therefore reasonable to use the Sr-Nd-Pb isotopes of the Cuoqen
436 dacites to represent the Lhasa basement. The constant $^{208}\text{Pb}/^{206}\text{Pb}$ values of clinopyroxene
437 crystallized at 590–935 MPa preclude any significant contamination with the lower continental
438 crust ([Fig. 11](#)).

439 Disentangling mantle source heterogeneity from shallow crustal contamination by using
440 radiogenic isotopes alone is not straightforward. Zircons of the Baingoin S-type granites nearby
441 the study area, which were formed by anatexis of Lhasa sediment-rich upper crustal assemblages,

442 display markedly varied ϵ_{Hf} values (-21.36 to -0.02; [Hu et al., 2019](#)). Asthenospheric melts
443 assimilating upper crustal rocks will, therefore, crystallize zircons with high ϵ_{Hf} core and low ϵ_{Hf}
444 rim, though the degree of ϵ_{Hf} variation depends on the Hf isotopic composition and the amount of
445 sediment assimilated. However, both low and high ϵ_{Hf} cores are developed in the Aruo zircons,
446 and the Hf isotope composition changes irregularly ([Fig. 3](#)). Thus, it is unlikely the Hf variability
447 in zircon of Aruo intrusions resulted from mixing of asthenospheric and crustal component.
448 Additional supports for this view include: (1) ancient xenocrystic zircons are absent in the Aruo
449 intrusions, yet our binary mixing modeling implies assimilation of a considerable amount (30–
450 50%) of upper crustal sediment would be needed to achieve the low $\epsilon_{\text{Nd}}(t)$ values and Th/Nb and
451 Th/ La ratios of the Aruo rocks ([Figs. 9c–9d](#)). Such large-scale assimilation would undoubtedly
452 leave petrological traces that are not witnessed in these rocks. (2) The whole-rock $\epsilon_{\text{Nd}}(t)$ values of
453 the Aruo intrusions remain constant or even slightly higher with increasing SiO₂ contents, at odds
454 with the trend of assimilation of an ancient crustal component ([Fig. 9a](#)). (3) There are no
455 correlations between the Hf isotopes and key trace element concentrations in zircon that are
456 sensitive to physicochemical variations, for example Th/U ratios and Hf contents for the degree of
457 magma differentiation and temperature, Yb/Gd for crystallization depth ([Fig. S2](#); e.g., [Kemp et al.,](#)
458 [2007](#); [Barth et al., 2013](#); [Cooper et al. 2014](#); [Grimes et al., 2015](#)).

459 The spread of data within Hf-O isotope space provides an independent means of assessing
460 mixtures of crustal and mantle reservoirs ([Roberts et al., 2013](#)). The zircon oxygen isotopes are
461 relatively uniform, albeit they are slightly higher than pristine mantle values and thus provide
462 further evidence of incorporation of supra-crustal materials into the petrogenetic process (e.g.,
463 [Valley et al., 2005](#)). Given that oxygen concentrations in sediments, crust and mantle are broadly
464 similar, the shape of mixing/assimilation curves on a Hf-O plot is largely controlled by the Hf
465 concentrations of the various components. The lack of covariation between Hf and O isotopes
466 from the same grains by the Aruo zircons ([Fig. 5b](#)) suggests the mixed components have
467 contrasting Hf concentrations (i.e., depleted mantle and sediment rather than basaltic melt and
468 sediment). The elevated $\delta^{18}\text{O}$ of high ϵ_{Hf} zircon suggests introduction of a high $\delta^{18}\text{O}$ component
469 relatively early on in magma differentiation ([Valley et al., 2005](#); [Kemp et al., 2007](#)), that is, to the
470 mantle source region. The lower $^{207}\text{Pb}/^{206}\text{Pb}$ and $^{208}\text{Pb}/^{206}\text{Pb}$ isotopic values of the Aruo
471 clinopyroxenes than that of the Neo-Tethyan ophiolite further support the interpretation that

472 recycled sediment was incorporated into the depleted mantle (Fig. 11c). Besides, the high whole-
473 rock Th/La ratios (>0.29 ; Table S5) and their negative relationship with the Sm/La ratios (not
474 shown), are consistent with the results of sediment-mantle mixing (Plank, 2005). Our modeling
475 shows that partial melting of asthenosphere mantle with the addition of 1–4% terrigenous
476 sediment can explain well the Hf-O isotope variability of the Aruo zircons (Fig. 5b). We note,
477 however, that we must explain why the whole-rock trace element and Nd isotopes distributions, as
478 well as Pb isotopes of clinopyroxene of the Aruo intrusions are relatively uniform (Figs. 8, 9 and
479 11). These phenomena argue that the amounts of recycled sediments are probably not the primary
480 control of the Hf isotope variation. The Hf concentrations and isotopes of subducted terrestrial
481 sediments are primarily controlled by zircon (e.g., Carpentier et al., 2009; Nebel et al. 2011),
482 which themselves may be heterogeneous in Hf isotopes as regionally manifested by the Baingoin
483 S-type granites described above (Hu et al., 2019). Zircon, however, contributes little Nd and Pb to
484 the whole rock budget compared to Zr and Hf. Thus, we argue that zircons in subducted sediments
485 were fully dissolved, and the Hf isotopes of the dissolved crystals governed the Hf isotopic
486 signature of the metasomatized mantle with negligible influence on Nd-Pb isotopes and most other
487 trace elements. Although the true composition of subducted sediments in this area is unknown, the
488 Lhasa Terrane suffered several phases of oceanic slab subduction and continental collision prior to
489 and during its assembly with the Gondwana supercontinent. We suggest that this complex history
490 justifies the variability in Hf isotopes of detrital zircon from Paleozoic-Mesozoic sediments (e.g.,
491 Zhu et al., 2009). Accordingly, we propose that the Hf isotope heterogeneity in zircon of Aruo
492 intrusions most likely was inherited from a mantle source metasomatically enriched with Hf from
493 sedimentary sources like those from which the Baingoin S-type granites were formed.

494

495 **Implications**

496 Our study has two main major implications, one is related to the regional tectonic evolution,
497 the other is more general and concerns the use of zircon Hf isotope data to trace magmatic
498 evolution and the growth of continental crust.

499 **Regional tectonic evolution**

500 Prior to the India-Asia collision, the Andean-type subduction of Neo-Tethyan lithosphere
501 along the southern margin of Lhasa Terrane formed prolonged Mesozoic magmatism with several

502 phases of flare-up (Ji et al., 2009). The underplating of depleted mantle-derived materials during
503 the oceanic slab subduction led to the growth of large amounts of juvenile crust in the southern
504 Lhasa Terrane (e.g., Ma et al., 2013a; Zhu et al., 2017). However, the tectonomagmatic evolution
505 of the central-north Lhasa Terrane remains enigmatic, although widespread Early Cretaceous
506 magmatism with a flare-up at ca. 120–110 Ma has been identified (e.g., Zhang et al., 2012; Li et
507 al. 2018; Zeng et al., 2020). Previous studies focused on intermediate-felsic magmatic rocks with
508 relatively little attention to contemporaneous mantle-derived mafic rocks, given their rare
509 exposure in the central Lhasa Terrane.

510 Three competing hypotheses have been proposed to explain the Early Cretaceous
511 tectonomagmatic evolution of the central-north Lhasa Terrane: (1) intra-block underthrusting
512 and/or post-collision lithospheric delamination following the collision between Lhasa and
513 Qiangtang terranes (Hu et al., 2017); (2) southward subduction, roll-back and eventually break-off
514 of the Bangong-Nujiang Oceanic lithosphere (Wang et al., 2020); (3) northward subduction and
515 roll-back of the Neo-Tethyan lithosphere (e.g., Zhang et al., 2012; Ma et al., 2013b; Zeng et al.,
516 2020). The low-K tholeiitic to calc-alkaline evolutionary trend (Fig. 6b), the negative Nb-Ta
517 anomalies with enrichment in most LILEs (Fig. 8), and the presence of amphibole crystals and
518 high melt H₂O contents of the studied Aruo dolerites and diorites are characteristic of arc-type
519 rocks (Zhou et al., 2006), and accordingly are more in support of their formation in a subduction-
520 related, rather than post-collisional setting. Moreover, zircon Hf-O isotopes and whole-rock Th/La
521 ratios and Nd isotopes (Figs. 5 and 9) collectively suggest the recycling of terrigenous sediments
522 into the depleted mantle. The lack of negative Zr-Hf anomalies (Fig. 8), together with the
523 suprachondritic Zr/Hf (34.3–41.2) and Zr/Y (5.0–7.0) ratios of the Aruo intrusions, imply that the
524 zircons in the subducted sediments might have been completely destroyed.

525 The dissolution of zircon in a sediment-derived melt is governed by zircon saturation (i.e., Zr
526 solubility in the melt, which increases with temperature and possibly decreases with pressure;
527 Watson and Harrison, 1983; Rubatto and Hermann, 2007). Melting experiments using sedimentary
528 starting materials show that temperatures in excess of 925 °C are needed to fully dissolve zircon
529 (Hermann and Rubatto, 2009). This is why mafic arc rocks with high Zr/Y ratios and positive Zr-
530 Hf anomalies are rare and are mainly found in hot subduction zones (e.g., the high Zr/Y basalts
531 from the Sumisu Rift, Hirai et al., 2018). For the Aruo intrusions, a special tectonic environment

532 therefore is inferred to gain slab surface temperature high enough to dissolve zircon in subducted
533 sediments, regardless of whether the sediment is carried by a Neo-Tethyan slab or Bangong
534 Tethyan slab. Based on a synthesis of independent observations, we (Zeng et al., 2020) have
535 recently proposed a model of steepening and roll-back of flatly northwards subducted Neo-
536 Tethyan oceanic lithosphere at ca.120–110Ma to explain the observed late Early Cretaceous
537 tectonic-magmatic complexity (Fig. 13). These observation are (Fig. 12): (1) Jurassic-Early
538 Cretaceous magmatism migrated northward throughout the Lhasa terrane and finally migrated
539 southward at ~110 Ma; (2) rapid cooling of the Xiabie and Baingoin granites started at ~120 Ma,
540 (Kapp et al., 2007; Volkmer et al., 2014); (3) deposition in the Coqen Basin of limestone of the
541 Langshan Formation and limestone to clastic red beds of the Takena Formation took place at ca.
542 113–96 Ma and ca. 105–90 Ma, respectively (Fig. 12; Sun et al., 2015, Leier et al., 2007); (4) no
543 southward subduction-related accretionary complex is preserved in the northern Lhasa Terrane
544 (Hu et al., 2022). The Aruo intrusions provide new evidence of a change in the tectonic regime of
545 the central-northern Lhasa Terrane at ca. 120 Ma. We propose that the rising asthenosphere in
546 response to the change in the Neo-Tethyan subduction angle could provide the additional heat
547 required to dissolve zircon in the subducted sediments as manifested by the geochemistry of the
548 Aruo intrusions (Fig. 13).

549

550 **The use of zircon Hf isotopes to track magmatic evolution and crust growth**

551 Our study reports substantial Hf isotope variation in zircon crystallized from mantle-derived
552 magma that requires a source containing components of depleted asthenosphere and pre-existing
553 mature crust. Our combined clinopyroxene and whole-rock chemical and isotopic investigation
554 limits contamination or mixing of crust-derived melts with mantle-derived melts in the upper crust
555 as the cause of heterogeneous Hf isotopes. Instead, we suggest that the heterogeneity was inherited
556 through metasomatism of depleted asthenospheric mantle by terrestrial sediments. Magmas
557 derived from these sources may pass this Hf isotope heterogeneity on to granitoids either by
558 fractional crystallization or by partially melting, which may be misunderstood as evidence of
559 magma mixing or disequilibrium melting of the crust if only zircon Hf isotopes in granitoids are
560 studied. Therefore, we emphasize the necessity of isotopic investigations on minerals crystallizing
561 before zircons, and combined O isotopic and whole-rock data, to correctly resolve the mechanism

562 of recycling of pre-existing continental crust to the source of arc rocks as shown by complex
563 zircon Hf isotopes.

564 In addition, our study provides the first evidence to show that the increasing zircon Hf
565 isotope values of Early Cretaceous magmatic rocks at ca. 120 Ma (Fig. 12) was related to
566 underplating of depleted mantle-derived materials, namely juvenile continental crustal growth.
567 Because of the addition of terrestrial sediments to the wedge mantle, the Hf isotopic model ages
568 (258–1224 Ma) are much older than the formation of this juvenile crust. Importantly, although
569 regional geological and geochemical data do provide testimony of crustal growth (Fig. 5), even
570 some of the zircons in the Aruo dolerites and diorites with MORB-like depleted Hf isotopes will
571 probably be omitted as evidence of continental crustal growth following the landmark criterion
572 ($\delta^{18}\text{O} + 5.9\%$ in 2σ level) proposed by Kemp et al. (2007). We therefore hold a conservative view
573 on simply using detrital zircon Hf-O isotopes to infer the timing and rate of continental crustal
574 growth through time regionally and globally, which certainly is useful but should be accompanied
575 with other additional constraints either from zircons themselves (e.g., the Th/Nb ratios as a proxy
576 of melt SiO_2 content; Turner et al., 2020) or minerals crystallized before zircons.

577

578 **Acknowledgments**

579 We are grateful to Christopher Spencer and an anonymous reviewer for their insightful reviews,
580 and to Paul Tomascak for his excellent editorial work, which substantially improved the
581 manuscript. Assistance from Ding-Shuai Xue, Dan-Ping Zhang, Bing-Yu Gao, Wen-Jun Li, Yong-
582 Hai Yuan, Hong-Xia Yu, Zheng-Lin Li, Yin-Hui Zhang, Le Zhang, Pei-Zhi Wang and Hao-Ran
583 Dou are sincerely acknowledged during the geochemical analyses. This research is supported by:
584 the Natural Science Foundation of China (42121002); the Second Tibetan Plateau Scientific
585 Expedition (STEP) program (2019QZKK0702); the Fundamental Research Funds for the Central
586 Universities (376202107 and 292019063); the National Key and Development Project of China
587 (2020YFA0714800); the Natural Science Foundation of China (92055208, 42273045 and
588 41903034), and the 111Project of the China Ministry of Science and Technology (BP0719021).
589 Ming-Jian Li is supported by a scholarship from the China Scholarship Council (202106400045).

590

References

- 591
592 Bao, Z.A., Zong, C.L., Fang, L.R., Yuan, H.L., Chen, K.Y., and Dai, M.N. (2018) Determination
593 of Hf–Sr–Nd isotopic ratios by MC-ICP-MS using rapid acid digestion after flux-free fusion
594 in geological materials. *Acta Geochimica*, 37, 244-256.
- 595 Barth, A.P., Wooden, J.L., Jacobson, C.E., and Economos, R.C. (2013) Detrital zircon as a proxy
596 for tracking the magmatic arc system: The California arc example. *Geology*, 41, 223-226.
- 597 Carpentier, M., Chauvel, C., Maury, R.C., and Mattielli, N. (2009) The “zircon effect” as recorded
598 by the chemical and Hf isotopic compositions of Lesser Antilles forearc sediments. *Earth and*
599 *Planetary Science Letters*, 287, 86-99.
- 600 Cooper, G.F., Wilson, C.J., Charlier, B.L., Wooden, J.L., and Ireland, T.R. (2014) Temporal
601 evolution and compositional signatures of two supervolcanic systems recorded in zircons
602 from Mangakino volcanic centre, New Zealand. *Contributions to Mineralogy and Petrology*,
603 167, 1-23.
- 604 Dilek, Y., and Furnes, H. (2011) Ophiolite genesis and global tectonics: Geochemical and tectonic
605 fingerprinting of ancient oceanic lithosphere. *Geological Society of America Bulletin*, 123, 387-
606 411.
- 607 Elburg, M., Vroon, P., van der Wagt, B., and Tchalikian, A. (2005) Sr and Pb isotopic composition
608 of five USGS glasses (BHVO-2G, BIR-1G, BCR-2G, TB-1G, NKT-1G). *Chemical Geology*,
609 223, 196-207.
- 610 Elhlou, S., Belousova, E., Griffin, W.L., Pearson, N.J., and O’Reilly, S.Y. (2006) Trace element
611 and isotopic composition of GJ-red zircon standard by laser ablation. *Geochimica et*
612 *Cosmochimica Acta*, 70, 158-158.
- 613 Ersoy, Y., and Helvacı, C. (2010) FC–AFC–FCA and mixing modeler: a Microsoft® Excel©
614 spreadsheet program for modeling geochemical differentiation of magma by crystal
615 fractionation, crustal assimilation and mixing. *Computers and Geosciences*, 36, 383-390.
- 616 Farina, F., Dini, A., Davies, J.H., Ovtcharova, M., Greber, N.D., Bouvier, A.S., Baumgartner, L.,
617 Ulianov, A., and Schaltegger, U. (2018) Zircon petrochronology reveals the timescale and
618 mechanism of anatectic magma formation. *Earth and Planetary Science Letters*, 495, 213-223.
- 619 Farina, F., Stevens, G., Gerdes, A., and Frei, D. (2014) Small-scale Hf isotopic variability in the Peninsula
620 pluton (South Africa): the processes that control inheritance of source $^{176}\text{Hf}/^{177}\text{Hf}$ diversity in S-type

- 621 granites. *Contributions to Mineralogy and Petrology*, 168, 1065.
- 622 Finch, M.A., Weinberg, R.F., Barrote, V.R., and Cawood, P.A. (2021) Hf isotopic ratios in zircon
623 reveal processes of anatexis and pluton construction. *Earth and Planetary Science Letters*,
624 576, 117215.
- 625 Fisher, C.M., Vervoort, J.D., and Hanchar, J.M. (2014) Guidelines for reporting zircon Hf isotopic
626 data by LA-MC-ICPMS and potential pitfalls in the interpretation of these data. *Chemical*
627 *Geology*, 363, 125-133.
- 628 Gasparon, M., Hilton, D.R., and Varne, R. (1994) Crustal contamination processes traced by helium
629 isotopes: Examples from the Sunda arc, Indonesia. *Earth and Planetary Science Letters*, 126, 15-22.
- 630 Ghiorso, M.S., and Sack, R.O. (1995) Chemical mass transfer in magmatic processes IV. A revised
631 and internally consistent thermodynamic model for the interpolation and extrapolation of
632 liquid-solid equilibria in magmatic systems at elevated temperatures and pressures.
633 *Contributions to Mineralogy and Petrology*, 119, 197-212.
- 634 Griffin, W.L., Pearson, N.J., Belousova, E., Jackson, S.V., Van Acherbergh, E., O'Reilly, S.Y., and
635 Shee, S.R. (2000) The Hf isotope composition of cratonic mantle: LAM-MC-ICPMS analysis
636 of zircon megacrysts in kimberlites. *Geochimica et Cosmochimica Acta*, 64, 133-147.
- 637 Grimes, C.B., Wooden, J.L., Cheadle, M.J., and John, B.E. (2015) "Fingerprinting" tectono-magmatic
638 provenance using trace elements in igneous zircon. *Contributions to Mineralogy and Petrology*, 170,
639 1-26.
- 640 Hastie, A.R., Kerr, A.C., Pearce, J.A., and Mitchell, S.F. (2007) Classification of altered volcanic
641 island arc rocks using immobile trace elements: development of the Th-Co discrimination
642 diagram. *Journal of Petrology*, 48, 2341-2357.
- 643 Hawkesworth, C.J., and Vollmer, R. (1979) Crustal contamination versus enriched mantle: $^{143}\text{Nd}/^{144}\text{Nd}$
644 and $^{87}\text{Sr}/^{86}\text{Sr}$ evidence from the Italian volcanics. *Contributions to Mineralogy and Petrology*, 69, 151-
645 165.
- 646 Hermann, J., and Rubatto, D. (2009) Accessory phase control on the trace element signature of
647 sediment melts in subduction zones. *Chemical Geology*, 265, 512-526.
- 648 Hirai, Y., Yoshida, T., Okamura, S., Tamura, Y., Sakamoto, I., and Shinjo, R. (2018) Breakdown of
649 residual zircon in the Izu arc subducting slab during backarc rifting. *Geology*, 46, 371-374.
- 650 Horstwood, M.S., Košler, J., Gehrels, G., Jackson, S.E., McLean, N.M., Paton, C., Pearson, N.J.,

- 651 Sircombe, K., Sylvester, P., Vermeesch, P., and Bowring, J.F. (2016) Community-derived
652 standards for LA-ICP-MS U-(Th)- Pb geochronology—Uncertainty propagation, age
653 interpretation and data reporting. *Geostandards and Geoanalytical Research*, 40, 311-332.
- 654 Hou, Z.Q., Duan, L.F., Lu, Y.J., Zheng, Y.C., Zhu, D.C., Yang, Z.M., Yang, Z.S., Wang, B.D., Pei,
655 Y.R., and Zhao, Z.D. (2015) Lithospheric architecture of the Lhasa terrane and its control on
656 ore deposits in the Himalayan-Tibetan orogen. *Economic Geology*, 110, 1541-1575.
- 657 Hu, P.Y., Zhai, Q.G., Jahn, B.M., Wang, J., Li, C., Chung, S.L., Lee, H.Y., and Tang, S.H. (2017)
658 Late Early Cretaceous magmatic rocks (118–113 Ma) in the middle segment of the Bangong-
659 Nuijiang suture zone, Tibetan Plateau: Evidence of lithospheric delamination. *Gondwana
660 Research*, 44, 116-138.
- 661 Hu, P.Y., Zhai, Q.G., Wang, J., Tang, Y., Wang, H.T., and Hou, K.J. (2018) Ediacaran magmatism
662 in the North Lhasa terrane, Tibet and its tectonic implications. *Precambrian Research*, 307,
663 137-154.
- 664 Hu, W.L., Wang, Q., Yang, J.H., Zhang, C., Tang, G.J., Ma, L., Qi, Y., Yang, Z.Y., and Sun, P.
665 (2019) Late early Cretaceous peraluminous biotite granites along the Bangong-Nuijiang
666 suture zone, Central Tibet: Products derived by partial melting of metasedimentary rocks?.
667 *Lithos*, 344, 147-158.
- 668 Hu, X.M., Ma, A.L., Xue, W.W., Garzanti, E., Cao, Y., Li, S.M., Sun, G.Y., and Lai, W. (2022)
669 Exploring a lost ocean in the Tibetan Plateau: Birth, growth, and demise of the Bangong-
670 Nuijiang Ocean. *Earth-Science Reviews*, 229, 104031.
- 671 Huang, Y., Zhao, Z., Zhu, D.C., Liu, Y., Liu, D., Zhou, Q., and Gao, S. (2017) The geochronologic
672 and geochemical constraints on the Early Cretaceous subduction magmatism in the central
673 Lhasa subterrane, Tibet. *Geological Journal*, 52, 463-475.
- 674 Ickert, R.B., Hiess, J., Williams, I.S., Holden, P., Ireland, T.R., Lanc, P., Schram, N., Foster, J.J.,
675 and Clement, S.W. (2008) Determining high precision, in situ, oxygen isotope ratios with a
676 SHRIMP II: Analyses of MPI-DING silicate-glass reference materials and zircon from
677 contrasting granites. *Chemical Geology*, 257, 114-128.
- 678 Jackson, S.E., Pearson, N.J., Griffin, W.L., and Belousova, E.A. (2004) The application of laser
679 ablation-inductively coupled plasma-mass spectrometry to in situ U-Pb zircon
680 geochronology. *Chemical Geology*, 211, 47-69.

- 681 Ji, W.Q., Wu, F.Y., Chung, S.L., Li, J.X., and Liu, C.Z. (2009) Zircon U–Pb geochronology and Hf
682 isotopic constraints on petrogenesis of the Gangdese batholith, southern Tibet. *Chemical*
683 *Geology*, 262, 229-245.
- 684 Kang Z.Q. (2009) Geochemistry, origin and tectonic implication of the Mesozoic volcanic rocks in
685 Lhasa block. A Dissertation Submitted to the Graduate School of the Chinese Academy of
686 Sciences for the Doctor Degree of Geochemistry.
- 687 Kang, Z.Q., Xu, J.F., Wilde, S.A., Feng, Z.H., Chen, J.L., Wang, B.D., Fu, W.C., and Pan, H.B.
688 (2014) Geochronology and geochemistry of the Sangri Group Volcanic Rocks, Southern
689 Lhasa Terrane: implications for the early subduction history of the Neo-Tethys and Gangdese
690 Magmatic Arc. *Lithos*, 200, 157-168.
- 691 Kapp, P., and DeCelles, P.G. (2019) Mesozoic–Cenozoic geological evolution of the Himalayan-
692 Tibetan orogen and working tectonic hypotheses. *American Journal of Science*, 319, 159-254.
- 693 Kapp, P., DeCelles, P.G., Gehrels, G.E., Heizler, M., and Ding, L. (2007) Geological records of the
694 Lhasa-Qiangtang and Indo-Asian collisions in the Nima area of central Tibet. *Geological*
695 *Society of America Bulletin*, 119, 917-933.
- 696 Kemp, A.I.S., Hawkesworth, C.J., Foster, G.L., Paterson, B.A., Woodhead, J.D., Hergt, J.M., Gray, C.M.,
697 and Whitehouse, M.J. (2007) Magmatic and crustal differentiation history of granitic rocks from Hf-O
698 isotopes in zircon. *Science*, 315, 980-983.
- 699 Kurtz, A.C., Derry, L.A., Chadwick, O.A., and Alfano, M.J. (2000) Refractory element mobility in
700 volcanic soils. *Geology*, 28, 683-686.
- 701 Leier, A.L., DeCelles, P.G., Kapp, P., and Ding, L. (2007) The Takena Formation of the Lhasa
702 terrane, southern Tibet: The record of a Late Cretaceous retroarc foreland basin. *Geological*
703 *Society of America Bulletin*, 119, 31-48.
- 704 Li, M.J., Zeng, Y.C., Xu, J.F., Huang, F., and Chen, Q. (2020) Petrogenesis of Early Jurassic (ca.
705 181 Ma) dacitic–rhyolitic volcanic rocks in the Amdo ophiolite mélange, central Tibetan
706 Plateau: Low-pressure partial melts of Bangong-Nujiang Tethys oceanic crust?. *Geological*
707 *Journal*, 55, 3283-3296.
- 708 Li, S.M., Wang, Q., Zhu, D.C., Stern, R.J., Cawood, P. A., Sui, Q. L., and Zhao, Z. (2018) One or
709 two Early Cretaceous arc systems in the Lhasa Terrane, southern Tibet. *Journal of*
710 *Geophysical Research: Solid Earth*, 123, 3391-3413.

- 711 Li, S.M., Zhu, D.C., Wang, Q., Zhao, Z.D., Sui, Q.L., Liu, S.A., Liu, D., and Mo, X.X. (2014)
712 Northward subduction of Bangong-Nujiang Tethys: insight from Late Jurassic intrusive rocks
713 from Bangong Tso in western Tibet. *Lithos*, 205, 284-297.
- 714 Li, X.H., Long, W.G., Li, Q.L., Liu, Y., Zheng, Y.F., Yang, Y.H., Chamberlain, K., Wan, D.F., and
715 Guo, C.H. (2010) Penglai zircon megacrysts: a potential new working reference material for
716 microbeam determination of Hf–O isotopes and U–Pb age. *Geostandards and Geoanalytical
717 Research*, 34, 117-134.
- 718 Li, X.H., Tang, G.Q., Gong, B., Yang, Y.H., Hou, K.J., Hu, Z.C., Li, Q.L., Liu, Y., and Li, W.X.
719 (2013) Qinghu zircon: A working reference for microbeam analysis of U–Pb age and Hf and
720 O isotopes. *Chinese Science Bulletin*, 58, 4647-4654.
- 721 Liu, Y.S., Hu, Z.C., Gao, S., Günther, D., Xu, J., Gao, C.G., and Chen, H.L. (2008) In situ analysis
722 of major and trace elements of anhydrous minerals by LA-ICP-MS without applying an
723 internal standard. *Chemical Geology*, 257, 34-43.
- 724 Ma, L., Wang, Q., Li, Z.X., Wyman, D.A., Jiang, Z.Q., Yang, J.H., Gou, G.N., and Guo, H.F.
725 (2013b) Early Late Cretaceous (ca. 93 Ma) norites and hornblendites in the Milin area,
726 eastern Gangdese: lithosphere–asthenosphere interaction during slab roll-back and an insight
727 into early Late Cretaceous (ca. 100–80 Ma) magmatic “flare-up” in southern Lhasa (Tibet).
728 *Lithos*, 172, 17-30.
- 729 Ma, L., Wang, Q., Wyman, D.A., Jiang, Z.Q., Yang, J.H., Li, Q.L., Gou, G.N., and Guo, H.F. (2013a)
730 Late Cretaceous crustal growth in the Gangdese area, southern Tibet: petrological and Sr–Nd–Hf–O
731 isotopic evidence from Zhengga diorite–gabbro. *Chemical Geology*, 349, 54-70.
- 732 Middlemost, E. A. (1994) Naming materials in the magma/igneous rock system. *Earth-Science
733 Reviews*, 37, 215-224.
- 734 Miyashiro, A. (1975) Volcanic rock series and tectonic setting. *Annual Review of Earth and
735 Planetary Sciences*, 3, 251-269.
- 736 Morimoto, N., Fabries, J., Ferguson, A.K., Ginzburg, I.V., Ross, M., Seifert, F.A., Zussman, J.,
737 Aoki, K., and Gottardi, G. (1988) Nomenclature of pyroxenes. *American Mineralogist*, 73,
738 1123-1133.
- 739 Nebel, O., Vroon, P.Z., van Westrenen, W., Iizuka, T., and Davies, G.R. (2011) The effect of
740 sediment recycling in subduction zones on the Hf isotope character of new arc crust, Banda

- 741 arc, Indonesia. *Earth and Planetary Science Letters*, 303, 240-250.
- 742 Pearce, J.A. (2014) Immobile element fingerprinting of ophiolites. *Elements*, 10, 101-108.
- 743 Plank, T. (2005) Constraints from thorium/lanthanum on sediment recycling at subduction zones
744 and the evolution of the continents. *Journal of Petrology*, 46, 921-944.
- 745 Putirka, K.D. (2008) Thermometers and barometers for volcanic systems. *Reviews in Mineralogy*
746 and *Geochemistry*, 69, 61-120.
- 747 Putirka, K.D., Mikaelian, H., Ryerson, F., and Shaw, H. (2003) New clinopyroxene-liquid
748 thermobarometers for mafic, evolved, and volatile-bearing lava compositions, with
749 applications to lavas from Tibet and the Snake River Plain, Idaho. *American Mineralogist*,
750 88, 1542-1554.
- 751 Qian, S.P., Ren, Z.Y., Richard, W., Zhang, L., Zhang, Y.H., Hong, L.B., Ding, X.L., and Wu, Y. D.
752 (2017) Petrogenesis of Early Cretaceous basaltic lavas from the North China Craton:
753 Implications for cratonic destruction. *Journal of Geophysical Research: Solid Earth*, 122,
754 1900-1918.
- 755 Ridolfi, F., Renzulli, A., and Puerini, M. (2010) Stability and chemical equilibrium of amphibole
756 in calc-alkaline magmas: an overview, new thermobarometric formulations and application to
757 subduction-related volcanoes. *Contributions to Mineralogy and Petrology*, 160, 45-66.
- 758 Roberts, N.M., Slagstad, T., Parrish, R.R., Norry, M.J., Marker, M., and Horstwood, M.S. (2013)
759 Sedimentary recycling in arc magmas: geochemical and U–Pb–Hf–O constraints on the
760 Mesoproterozoic Suldal Arc, SW Norway. *Contributions to Mineralogy and Petrology*, 165,
761 507-523.
- 762 Roeder, P.L., and Emslie, R. (1970) Olivine-liquid equilibrium. *Contributions to Mineralogy and*
763 *Petrology*, 29, 275-289.
- 764 Rubatto, D., and Hermann, J. (2007) Experimental zircon/melt and zircon/garnet trace element
765 partitioning and implications for the geochronology of crustal rocks. *Chemical Geology*, 241,
766 38-61.
- 767 Sláma, J., Košler, J., Condon, D.J., Crowley, J.L., Gerdes, A., Hanchar, J.M., Horstwood, M.S.A.,
768 Morris, G.A., Nasdala, L., Norberg, N., Schaltegger, U., Schoene, B., Tubrett, M.N.,
769 and Whitehouse, M.J. (2008) Plešovice zircon—a new natural reference material for U–Pb
770 and Hf isotopic microanalysis. *Chemical Geology*, 249, 1-35.

- 771 Spencer, C.J., Cavosie, A.J., Raub, T.D., Rollinson, H., Jeon, H., Searle, M.P., Miller, J.A.,
772 McDonald, B.J., and Evans, N.J. (2017) Evidence for melting mud in Earth's mantle from
773 extreme oxygen isotope signatures in zircon. *Geology*, 45, 975-978.
- 774 Spencer, C.J., Kirkland, C.L., Roberts, N.M.W., Evans, N.J., and Liebmann, J. (2020) Strategies
775 towards robust interpretations of in situ zircon Lu–Hf isotope analyses. *Geoscience Frontiers*,
776 11, 843-853.
- 777 Sun, G.Y., Hu, X., Sinclair, H.D., BouDagher-Fadel, M.K., and Wang, J. (2015) Late Cretaceous
778 evolution of the Coqen Basin (Lhasa terrane) and implications for early topographic growth
779 on the Tibetan Plateau. *Geological Society of America Bulletin*, 127, 1001-1020.
- 780 Sun, S.S., and McDonough, W.F. (1989) Chemical and isotopic systematics of oceanic basalts:
781 implications for mantle composition and processes. Geological Society, London, Special
782 Publications, 42, 313-345.
- 783 Tang, M., Wang, X.L., Shu, X.J., Wang, D., Yang, T., and Gopon, P. (2014) Hafnium isotopic
784 heterogeneity in zircons from granitic rocks: Geochemical evaluation and modeling of
785 “zircon effect” in crustal anatexis. *Earth and Planetary Science Letters*, 389, 188-199.
- 786 Tang, Y., Zhai, Q.G., Chung, S.L., Hu, P.Y., Wang, J., Xiao, X.C., Song, B., Wang, H.T., and Lee,
787 H.Y. (2020) First mid-ocean ridge-type ophiolite from the Meso-Tethys suture zone in the
788 north-central Tibetan plateau. *Geological Society of America Bulletin*, 132, 2202-2220.
- 789 Turner, S., Wilde, S., Wörner, G., Schaefer, B., and Lai, Y. J. (2020). An andesitic source for Jack
790 Hills zircon supports onset of plate tectonics in the Hadean. *Nature Communications*, 11, 1-5.
- 791 Valley, J.W. (2003) Oxygen isotopes in zircon. *Reviews in Mineralogy and Geochemistry*, 53,
792 343-385.
- 793 Valley, J.W., Lackey, J.S., Cavosie, A.J., Clechenko, C.C., Spicuzza, M.J., Basei, M.A.S., Bindeman, I.N.,
794 Ferreira, V.P., Sial, A.N., King, E.M., Peck, W.H., Sinha, A.K., and Wei, C.S. (2005) 4.4 billion years
795 of crustal maturation: oxygen isotope ratios of magmatic zircon. *Contributions to Mineralogy and
796 Petrology*, 150, 561-580.
- 797 Villaros, A., Buick, I.S., and Stevens, G. (2012) Isotopic variations in S-type granites: an inheritance from a
798 heterogeneous source?. *Contributions to Mineralogy and Petrology*, 163, 243-257.
- 799 Volkmer, J.E., Kapp, P., Horton, B.K., Gehrels, G.E., Minervini, J.M., and Ding, L. (2014)
800 Northern Lhasa thrust belt of central Tibet: Evidence of Cretaceous–early Cenozoic

- 801 shortening within a passive roof thrust system. Geological Society of America Special
802 Papers, 507, 59-70.
- 803 Wang, J.P., Yang, C.H., Lu, S.W., et al. (2002) 1:250,000 Regional Geological Survey Report of
804 the People's Republic of China (Nyima Sheet). Published by the Mapping Center Henan
805 Provincial Institute of Geological Survey.
- 806 Wang, W., Wang, M., Zhai, Q.G., Xie, C.M., Hu, P.Y., Li, C., Liu, J.H., and Luo, A.B. (2020)
807 Transition from oceanic subduction to continental collision recorded in the Bangong-Nujiang
808 suture zone: Insights from Early Cretaceous magmatic rocks in the north-central Tibet.
809 Gondwana Research, 78, 77-91.
- 810 Watson, E.B., and Harrison, T.M. (1983) Zircon saturation revisited: temperature and composition
811 effects in a variety of crustal magma types. Earth and Planetary Science Letters, 64, 295-304.
- 812 Weis, D., Kieffer, B., Maerschalk, C., Barling, J., de Jong, J., Williams, G.A., Hanano, D.,
813 Pretorius, W., Mattielli, N., Scoates, J.S., Goolaerts, A., Friedman, R.M., and Mahoney, J.B.
814 (2006) High-precision isotopic characterization of USGS reference materials by TIMS and
815 MC-ICP-MS. Geochemistry, Geophysics, Geosystems, 7(8).
- 816 Wu, F.Y., Yang, Y.H., Xie, L.W., Yang, J.H., and Xu, P. (2006) Hf isotopic compositions of the
817 standard zircons and baddeleyites used in U–Pb geochronology. Chemical Geology, 234,
818 105–126.
- 819 Xu, J.F., and Castillo, P.R. (2004) Geochemical and Nd–Pb isotopic characteristics of the Tethyan
820 asthenosphere: implications for the origin of the Indian Ocean mantle domain.
821 Tectonophysics, 393, 9-27.
- 822 Yin, A., and Harrison, T.M. (2000) Geologic evolution of the Himalayan-Tibetan orogen. Annual
823 Review of Earth and Planetary Sciences, 28, 211-280.
- 824 Zeng, Y.C., Chen, J.L., Xu, J.F., Wang, B.D., and Huang, F. (2016) Sediment melting during
825 subduction initiation: Geochronological and geochemical evidence from the Darutso high-
826 Mg andesites within ophiolite melange, central Tibet. Geochemistry, Geophysics,
827 Geosystems, 17, 4859-4877.
- 828 Zeng, Y.C., Xu, J.F., Chen, J.L., Wang, B.D., Huang, F., Xia, X.P., and Li, M.J. (2021a) Early
829 Cretaceous (~ 138–134 Ma) Forearc Ophiolite and Tectonomagmatic Patterns in Central
830 Tibet: Subduction Termination and Re-initiation of Meso-Tethys Ocean Caused by Collision

- 831 of an Oceanic Plateau at the Continental Margin?. *Tectonics*, 40, e2020TC006423.
- 832 Zeng, Y.C., Xu, J.F., Chen, J.L., Wang, B.D., Kang, Z.Q., and Huang, F. (2018) Geochronological
833 and geochemical constraints on the origin of the Yunzhug ophiolite in the Shiquanhe–
834 Yunzhug–Namu Tso ophiolite belt, Lhasa Terrane, Tibetan Plateau. *Lithos*, 300, 250-260.
- 835 Zeng, Y.C., Xu, J.F., Huang, F., Li, M.J., and Chen, Q. (2020) Generation of the 105–100 Ma Dagze
836 volcanic rocks in the north Lhasa Terrane by lower crustal melting at different temperature and depth:
837 Implications for tectonic transition. *Geological Society of America Bulletin*, 132, 1257-1272.
- 838 Zeng, Y.C., Xu, J.F., Li, M.J., Chen, J.L., Wang, B.D., Huang, F., and Ren, S.H. (2021b) Late
839 Eocene two-pyroxene trachydacites from the southern Qiangtang Terrane, central Tibetan
840 Plateau: High-temperature melting of overthickened and dehydrated lower crust. *Journal of*
841 *Petrology*, 62, egab080.
- 842 Zhang, K.J., Zhang, Y.X., Tang, X.C., and Xia, B. (2012) Late Mesozoic tectonic evolution and growth of
843 the Tibetan plateau prior to the Indo-Asian collision. *Earth-Science Reviews*, 114, 236-249.
- 844 Zhang, L., Ren, Z.Y., Nichols, A.R., Zhang, Y.H., Zhang, Y., Qian, S.P., and Liu, J.Q. (2014) Lead
845 isotope analysis of melt inclusions by LA-MC-ICP-MS. *Journal of Analytical Atomic*
846 *Spectrometry*, 29, 1393–1405.
- 847 Zhang, S.Q., Mahoney, J.J., Mo, X.X., Ghazi, A.M., Milani, L., Crawford, A.J., Guo, T.Y., and
848 Zhao, Z.D. (2005) Evidence for a widespread Tethyan upper mantle with Indian-Ocean-type
849 isotopic characteristics. *Journal of Petrology*, 46, 829-858.
- 850 Zhou, M.F., Ma, Y., Yan, D.P., Xia, X., Zhao, J.H., and Sun, M. (2006) The Yanbian terrane
851 (Southern Sichuan Province, SW China): a Neoproterozoic arc assemblage in the western
852 margin of the Yangtze block. *Precambrian Research*, 144, 19-38.
- 853 Zhou, X. (2017) Tectonic history and crustal evolution of the northern and central Lhasa Terrane.
854 A Dissertation Submitted to China University of Geosciences for the Doctor Degree of
855 Mineralogy, Petrology and Economic Geology.
- 856 Zhu, D. C., Zhao, Z. D., Niu, Y., Dilek, Y., and Mo, X. X. (2011b). Lhasa terrane in southern Tibet
857 came from Australia. *Geology*, 39(8), 727-730.
- 858 Zhu, D.C., Mo, X.X., Niu, Y., Zhao, Z.D., Wang, L.Q., Liu, Y.S., and Wu, F.Y. (2009)
859 Geochemical investigation of Early Cretaceous igneous rocks along an east–west traverse
860 throughout the central Lhasa Terrane, Tibet. *Chemical Geology*, 268, 298-312.

861 Zhu, D.C., Wang, Q., Cawood, P.A., Zhao, Z.D., and Mo, X.X. (2017) Raising the Gangdese mountains in
862 southern Tibet. *Journal of Geophysical Research: Solid Earth*, 122, 214-223.

863 Zhu, D.C., Zhao, Z.D., Niu, Y., Dilek, Y., Wang, Q., Ji, W.H., Dong, G.C., Sui, Q.L., Liu, Y.S.,
864 Yuan, H.L., and Mo, X.X. (2012) Cambrian bimodal volcanism in the Lhasa Terrane,
865 southern Tibet: record of an early Paleozoic Andean-type magmatic arc in the Australian
866 proto-Tethyan margin. *Chemical Geology*, 328, 290-308.

867 Zhu, D.C., Zhao, Z.D., Niu, Y., Mo, X.X., Chung, S.L., Hou, Z.Q., Wang, L.Q., and Wu, F.Y.
868 (2011a) The Lhasa Terrane: record of a microcontinent and its histories of drift and growth.
869 *Earth and Planetary Science Letters*, 301, 241-255.

870

871

Figure Captions:

872 Figure 1. (a) Simplified tectonic map of the Tibetan Plateau showing the distribution of Mesozoic
873 magmatic rocks of the Lhasa Terrane (after [Zeng et al., 2020](#)). (b) Geological map of the Aruo
874 region, central Lhasa Terrane. IYZSZ-Indus-Yarlung Zangbo Suture Zone; BSZ-Bangong Suture
875 Zone; SNMZ-Shiquanhe-NamuTso ophiolite mélangé zone; LMF-Lobuodui-Milashan Fault. The
876 zircon age (zircon U–Pb) of the Xainza basalts-dacites is from [Kang \(2009\)](#).

877

878 Figure 2. Representative photomicrographs (cross-polarized illumination) showing the mineral
879 assemblages of the Aruo dolerites (a-c) and diorites (d). Pl-plagioclase; Cpx-clinopyroxene; Amp-
880 amphibole; Ilm-ilmenite; Ep-epidote.

881

882 Figure 3. Representative cathodoluminescence (CL) images showing the morphology, $^{206}\text{Pb}/^{238}\text{U}$
883 age (Ma), and Hf-O isotopes of the zircon crystals in the Aruo dolerites and diorites.

884

885 Figure 4. (a-c) Zircon U-Pb concordia diagrams of the Aruo dolerites and diorites, (d) chondrite-
886 normalized zircon rare earth element patterns for the Aruo dolerites and diorites (normalizing
887 values are from [Sun and McDonough, 1989](#)).

888

889 Figure 5. Plots of (a) zircon age vs $\epsilon_{\text{Hf}}(t)$ and (b) zircon $\epsilon_{\text{Hf}}(t)$ vs $\delta^{18}\text{O}$. In (b) the curves are binary
890 mixtures of putative mantle and crustal end-members (upper continental crust). The basalt was

891 represented by the Jurassic MORB-type rock (15T160) in the Ren Co region (Tang et al., 2020),
892 and the upper crust was represented by the Baingoin S-type granite (16BG50-5; Hu et al., 2019).
893 Mixing with upper continental crust with different $\delta^{18}\text{O}$ values is modeled given the substantially
894 varied zircon $\delta^{18}\text{O}$ values of the Baingoin S-type granites (Hu et al., 2019), and a mantle end-
895 member with moderately elevated $\delta^{18}\text{O}$ value is assumed and modeled because the zircons in the
896 Aruo intrusions with asthenosphere-like $\varepsilon_{\text{HF}}(t)$ values also display $\delta^{18}\text{O}$ value higher than those in
897 equilibrium with mantle-derived magmas (e.g., Roberts et al., 2013).

898

899 Figure 6. (a) $\text{Na}_2\text{O} + \text{K}_2\text{O}$ versus SiO_2 (Middlemost, 1994); (b) SiO_2 vs. FeO_t/MgO diagram (after
900 Miyashiro, 1975) showing data of the Aruo intrusions. The data of the nearby Xainza basalts-
901 dacites are plotted here and in the following geochemical diagrams for comparison because they
902 were formed synchronously with the Aruo intrusions (Fig. 1; Kang, 2009).

903

904 Figure 7. (a-f) Harker diagrams showing CaO , Al_2O_3 , TiO_2 , $\text{Fe}_2\text{O}_3^{\text{T}}$, MgO and K_2O versus SiO_2 for
905 the Aruo intrusions. The dashed and solid lines represent the MELTS simulated fractional
906 crystallization trends of magma evolution (Ghiorso and Sack, 1995). The model assumes that the
907 initial magma composition is a dolerite sample 19AR-05, the water content is +3 wt. %, the
908 pressure is 200 MPa, and $f_{\text{O}_2} = \Delta\text{QFM} \sim \Delta\text{QFM} + 1$. The data of the Xainza basalts-dacites are from
909 Kang (2009).

910

911 Figure 8. (a) Primitive mantle-normalized trace element patterns and (b) chondrite-normalized
912 rare earth element data for the Aruo intrusions. Normalizing values are from Sun and McDonough
913 (1989). The data of the Xainza basalts-dacites are from Kang (2009).

914

915 Figure 9. Plots of (a) whole-rock SiO_2 vs $\varepsilon_{\text{Nd}}(t)$, (b) Th/Nb versus $\varepsilon_{\text{Nd}}(t)$, and (c) Th/La versus
916 $\varepsilon_{\text{Nd}}(t)$ for the Aruo intrusions. The AFC simulation was performed using the method described by
917 Ersoy and Helvacı (2010); “r” refers to the assimilation rate in AFC models. In Fig. b, the
918 assimilated end-member is represented by one sample of the Baingoin S-type granites (16BG49-2;
919 Hu et al., 2019), and the depleted end-member is the Jurassic Ren Co MORB-type rock (sample
920 15T269; Tang et al., 2020). The data of lithospheric mantle-derived gabbros are from Zhu et al.

921 (2012) and Hu et al. (2018), and of the Xainza basalts-dacites are from Kang (2009).

922

923 Figure 10. (a) $\text{CaSiO}_3\text{-MgSiO}_3\text{-FeSiO}_3$ diagram showing the compositions of pyroxene
924 (Morimoto et al., 1988), (b) plot of clinopyroxene $\text{Mg}^\#$ vs. whole-rock $\text{Mg}^\#$ values, showing the
925 melt-clinopyroxene equilibrium band, (c-d) primitive mantle-normalized multi-element patterns
926 and chondrite-normalized REE patterns for clinopyroxenes of the Aruo dolerites and diorites.

927

928 Figure 11. Plots of (a) Al_2O_3 versus $\text{Mg}^\#$ values, (b) Sr versus $\text{Mg}^\#$ values, (c) $(^{208}\text{Pb}/^{206}\text{Pb})_i$
929 versus $(^{207}\text{Pb}/^{206}\text{Pb})_i$, and (d) $(^{207}\text{Pb}/^{206}\text{Pb})_i$ versus $\text{Mg}^\#$ values for clinopyroxene from the Aruo
930 intrusions. The data of Neo-Tethyan ophiolite are from Xu and Castillo (2004) and Zhang et al.
931 (2005), and of the ancient basement are inferred from Huang et al. (2017). The field of sediment is
932 from Qian et al. (2017).

933

934 Figure 12. Temporal and spatial distribution of Mesozoic magmatic rocks in the Lhasa Terrane
935 (after Zeng et al., 2020 and references therein). The zircon $\varepsilon_{\text{Hf}}(t)$ values of magmatic rocks in the
936 central Lhasa Terrane notably increase at ca. 120 Ma. IYZSZ—Indus-Yarlung Zangbo Suture
937 Zone; BSZ—Bangong Suture Zone; SNMZ—ShiquanheNamuTso ophiolite mélange zone;
938 LMF—Lobuodui-Milashan Fault.

939

940 Figure 13. Schematic model of the genesis of the Aruo intrusions. The subduction-derived melts
941 incorporate Hf derived from heterogeneous detrital zircon components. Without effectively
942 mixing, these components crystallize magmatic zircon that captures this sedimentary
943 heterogeneity.

944

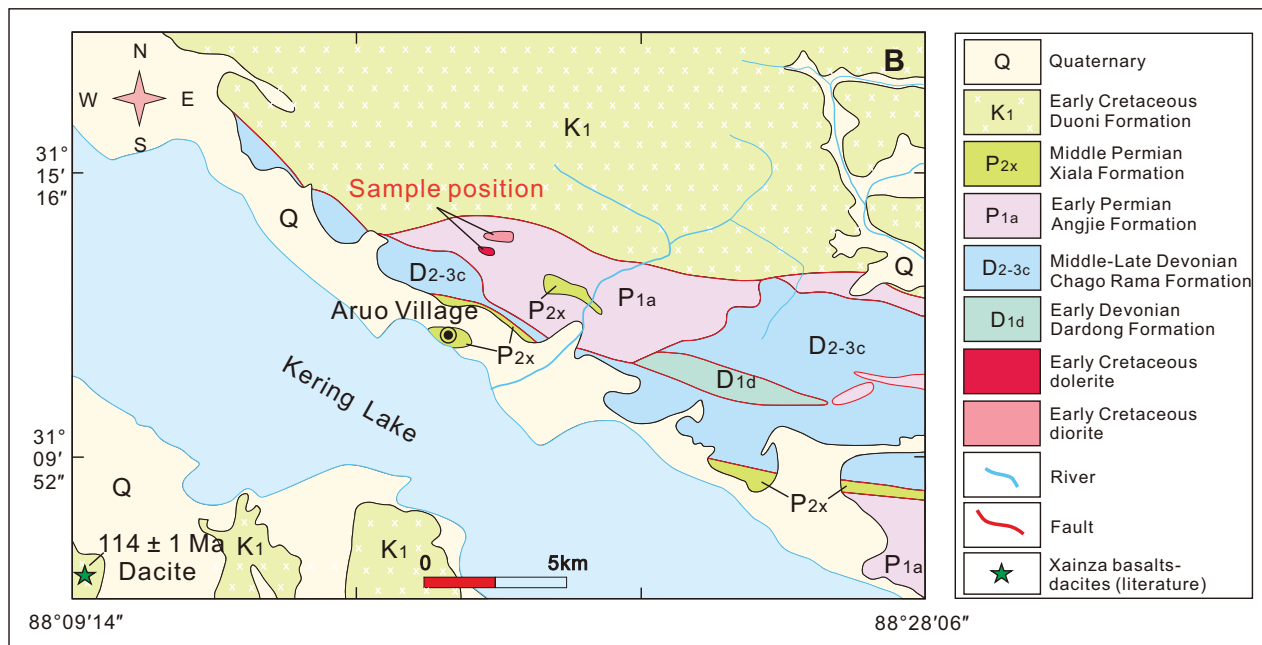
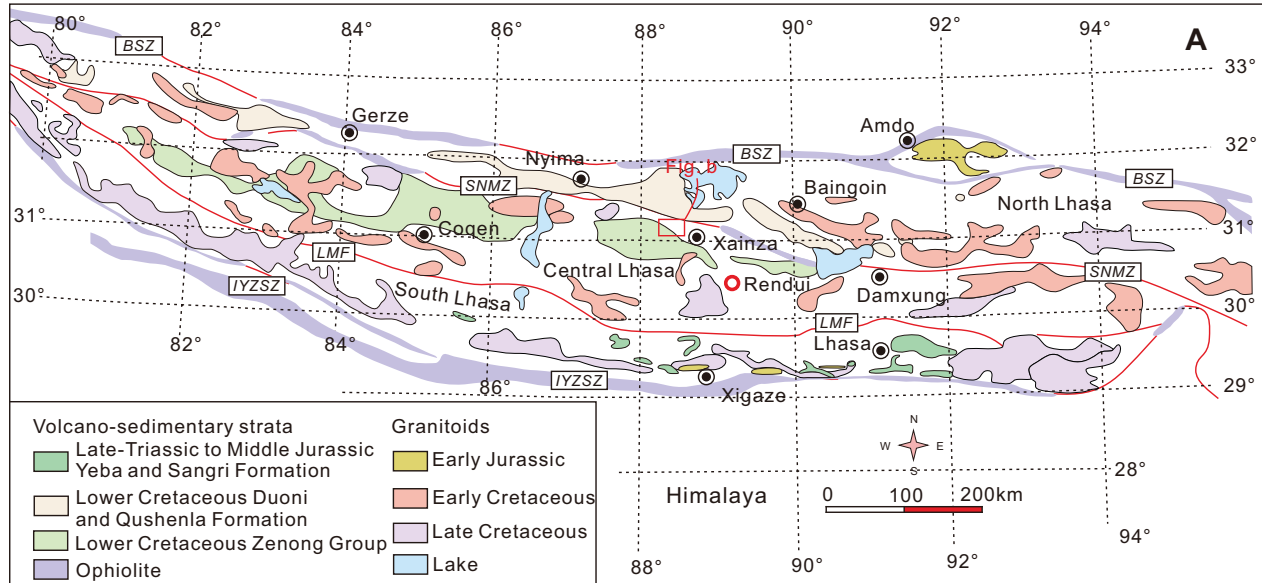


Figure 1

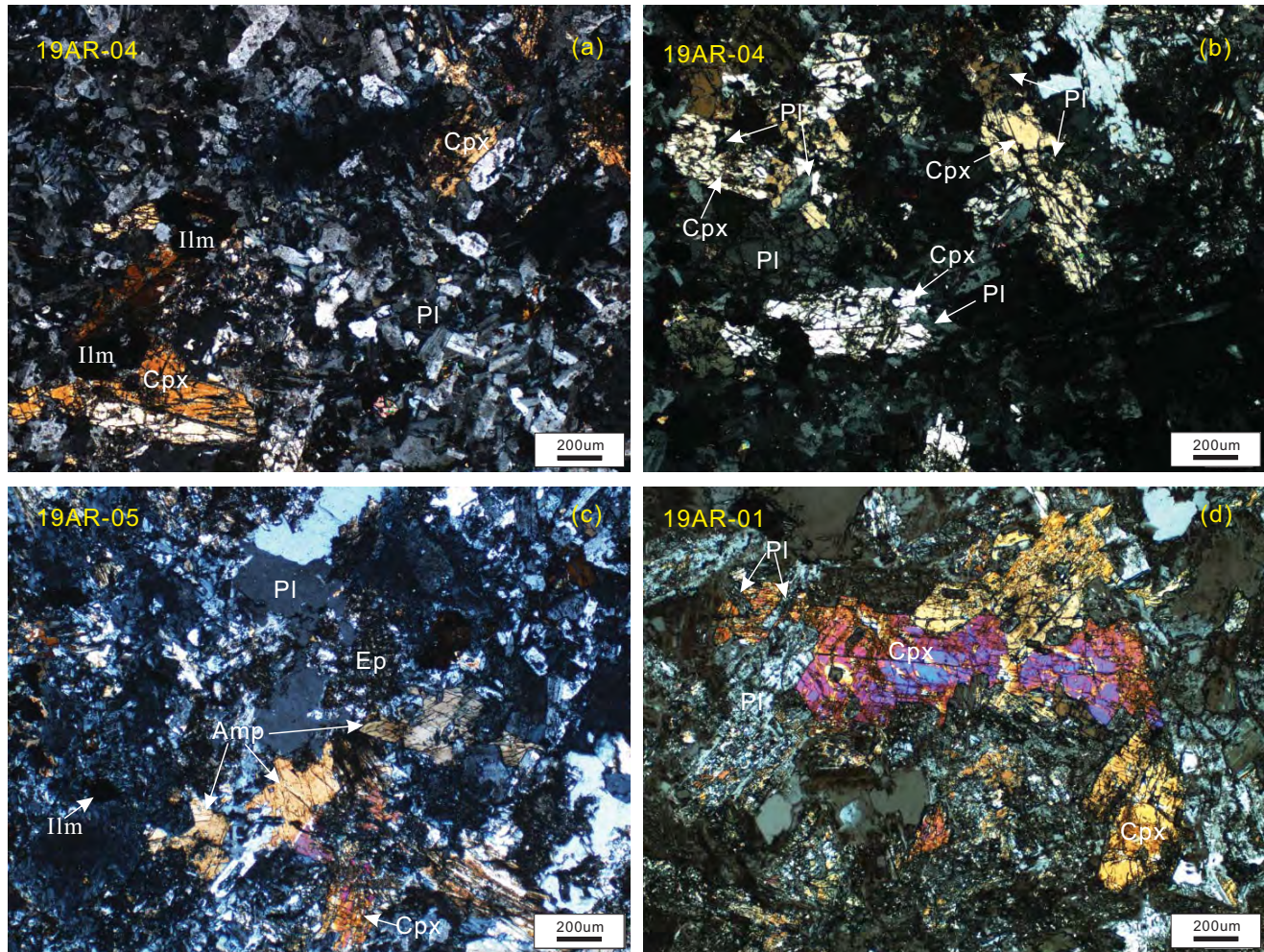


Figure 2

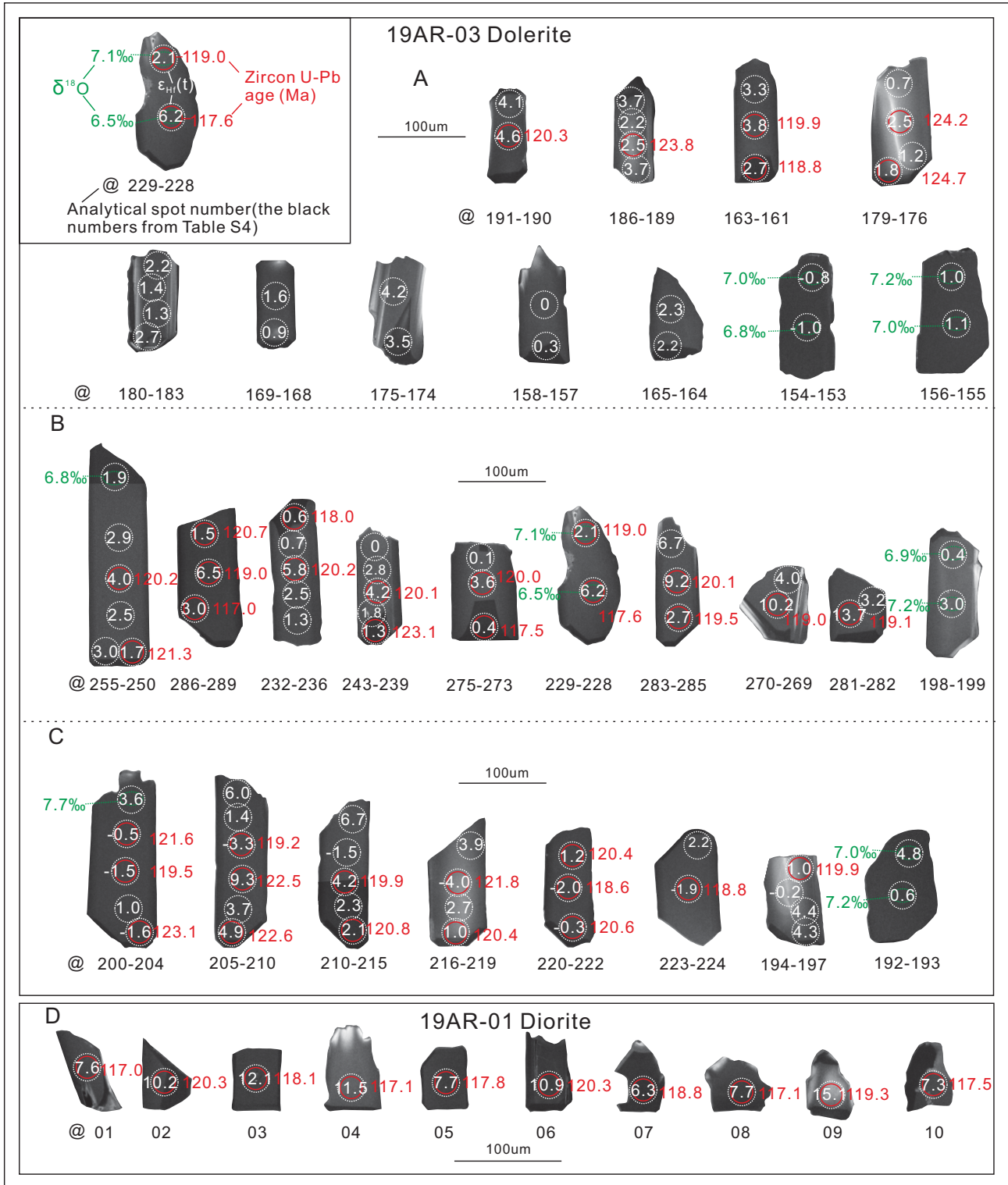


Figure 3

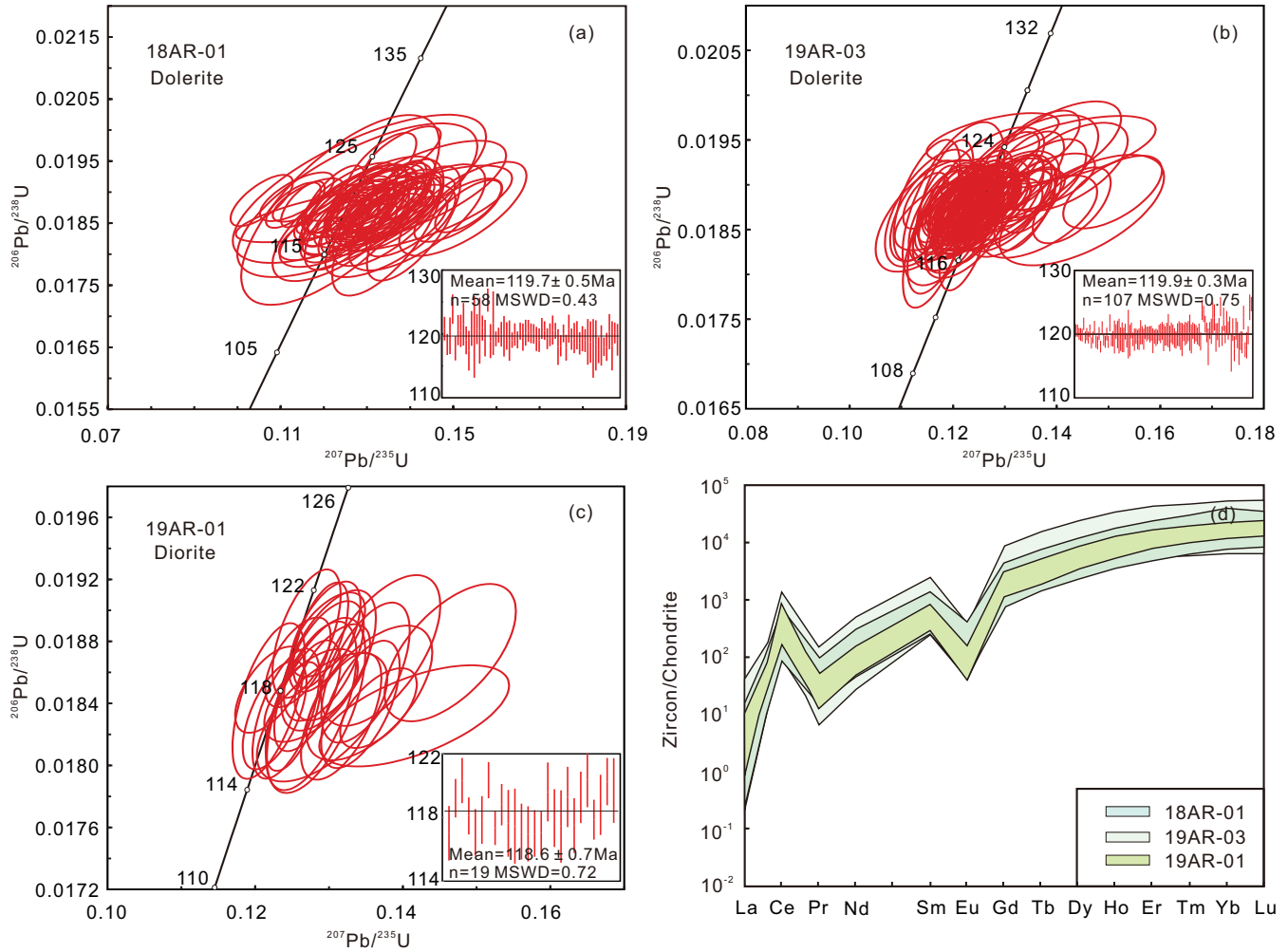


Figure 4

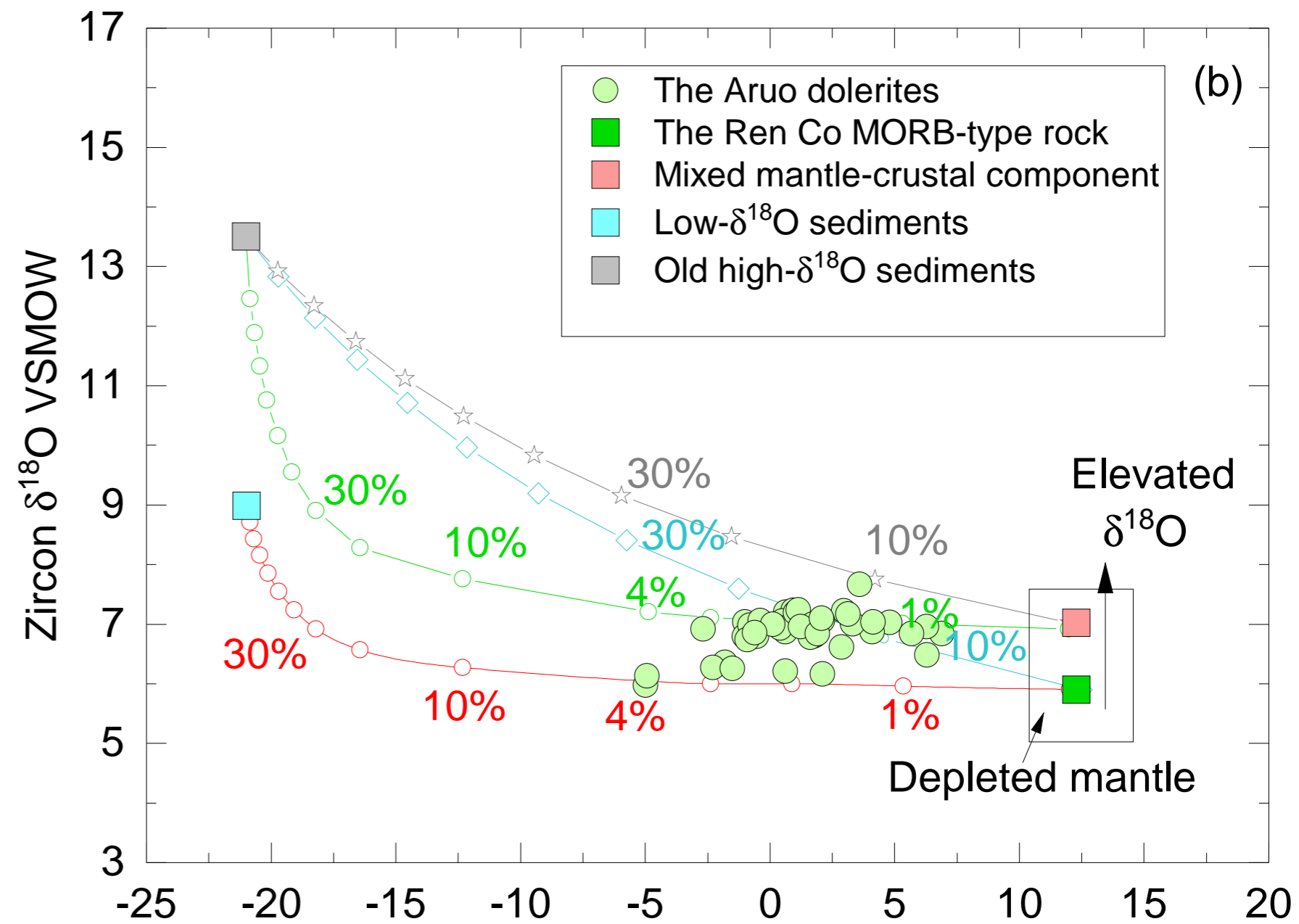
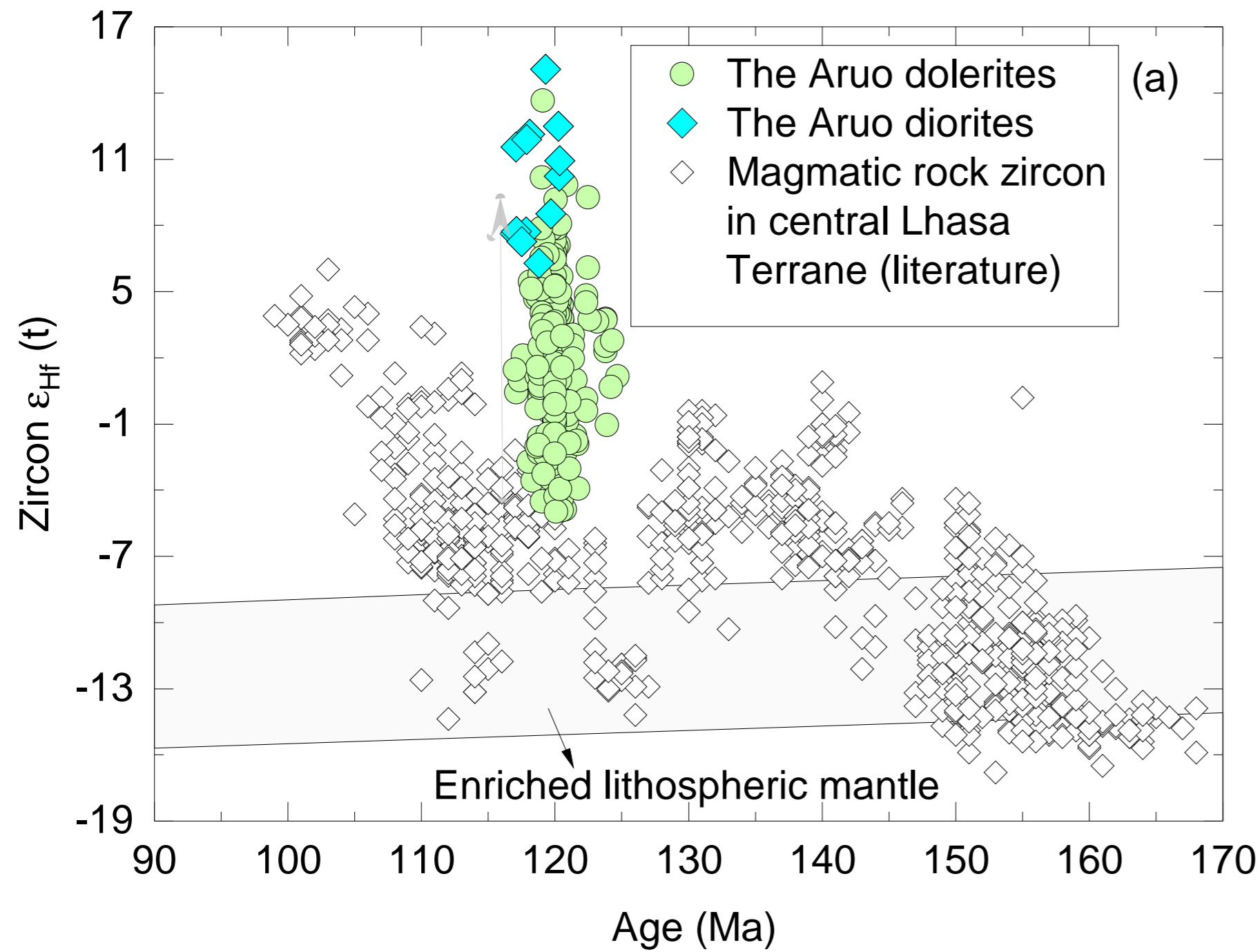


Figure 5

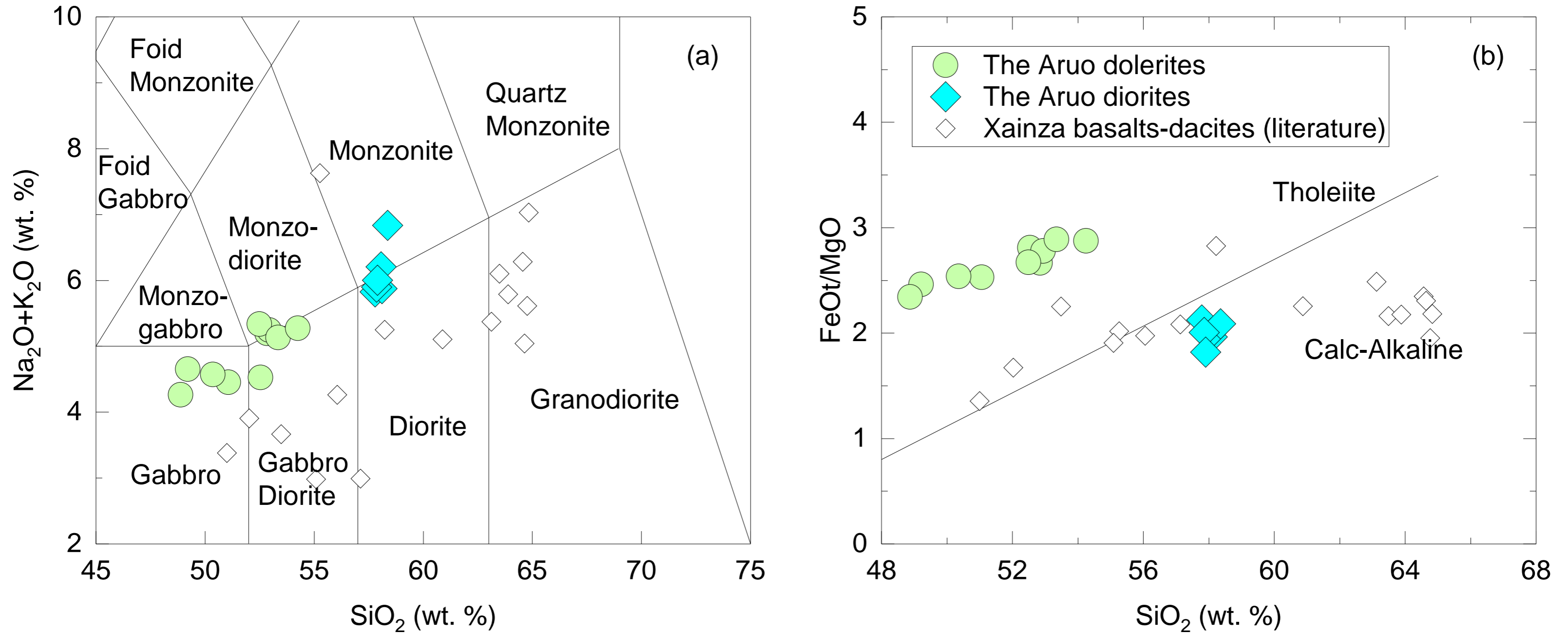


Figure 6

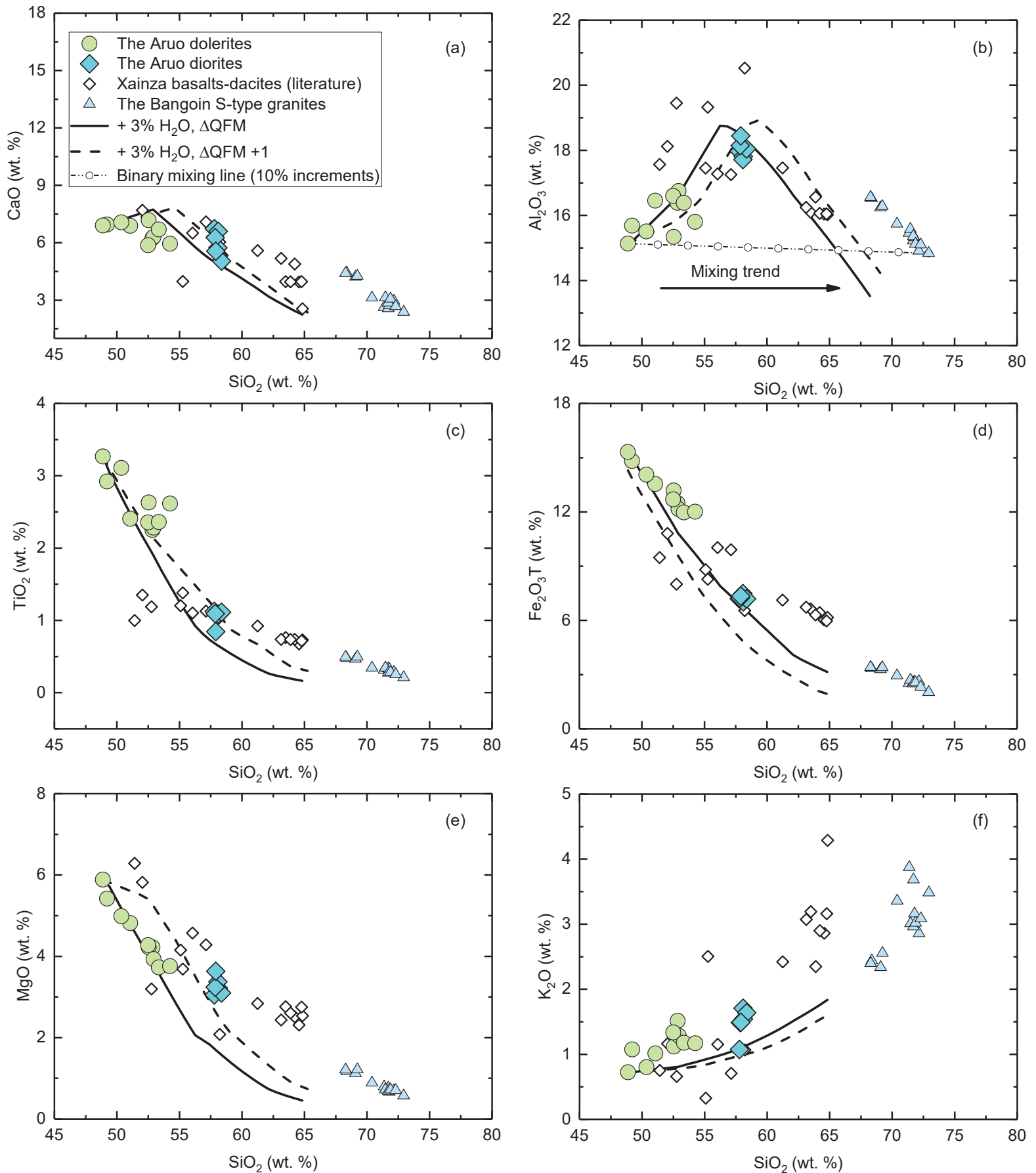


Figure 7

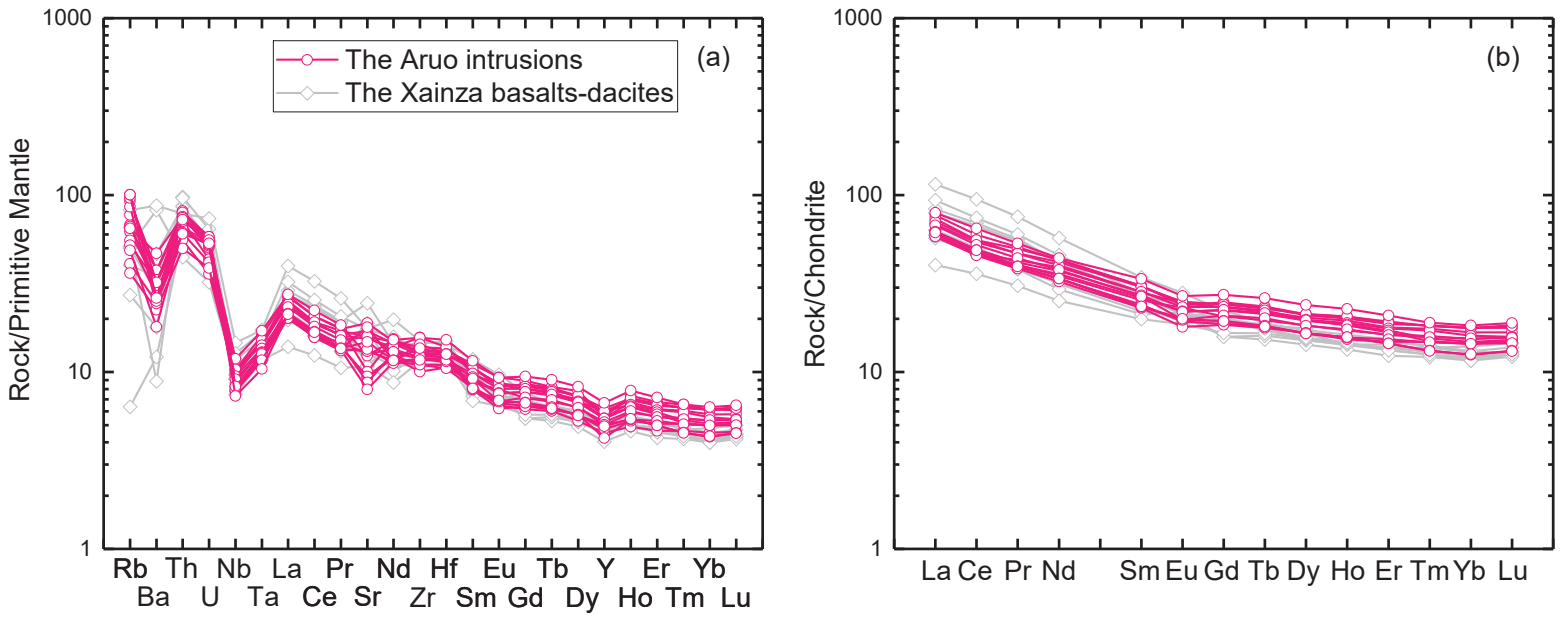


Figure 8

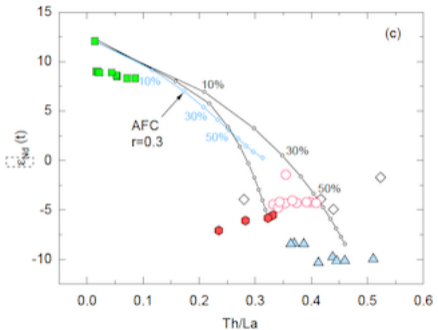
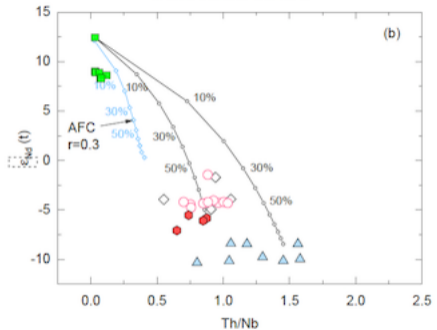
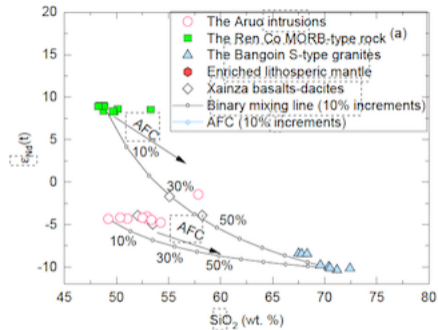


Figure 9

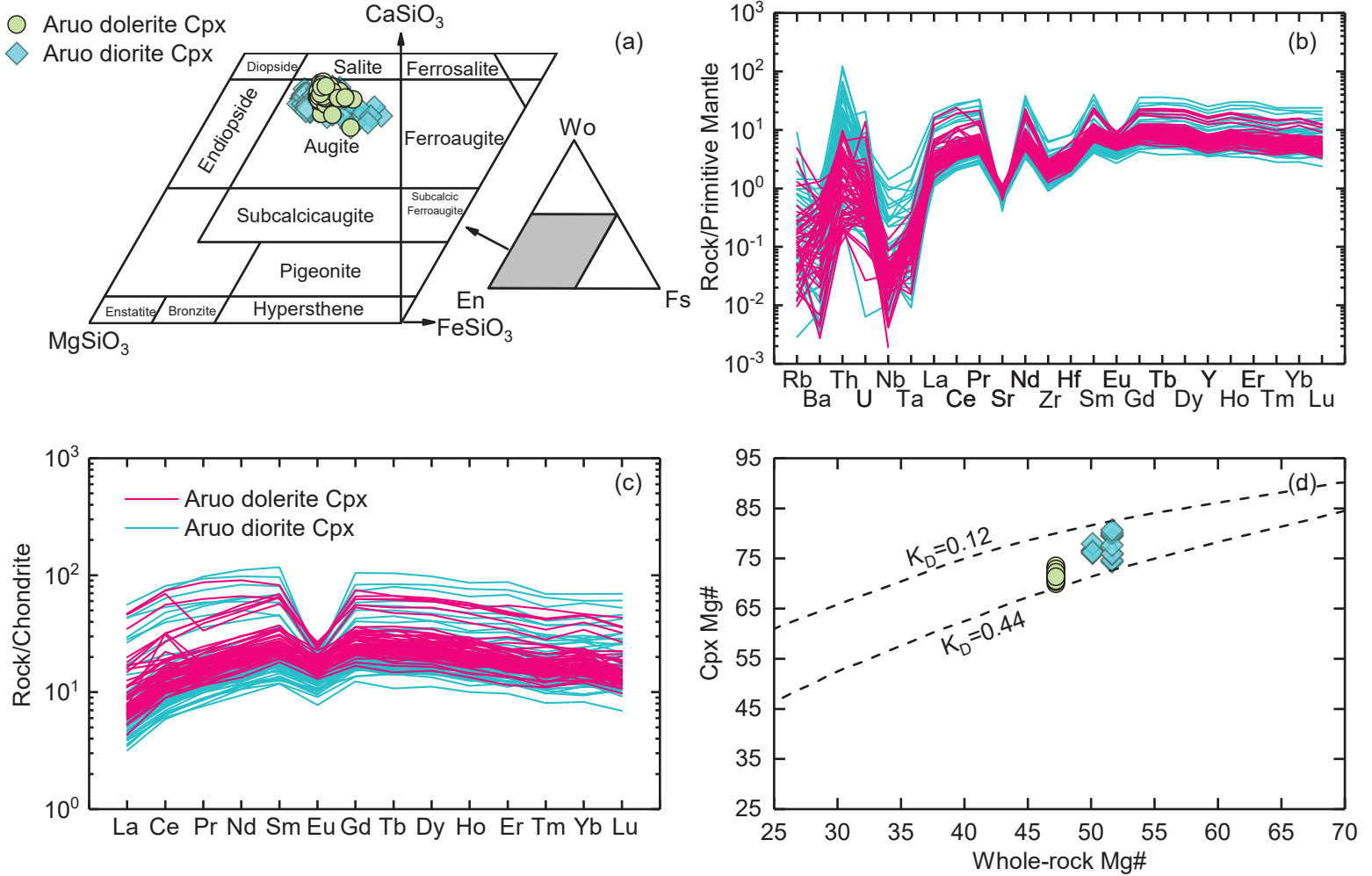


Figure 10

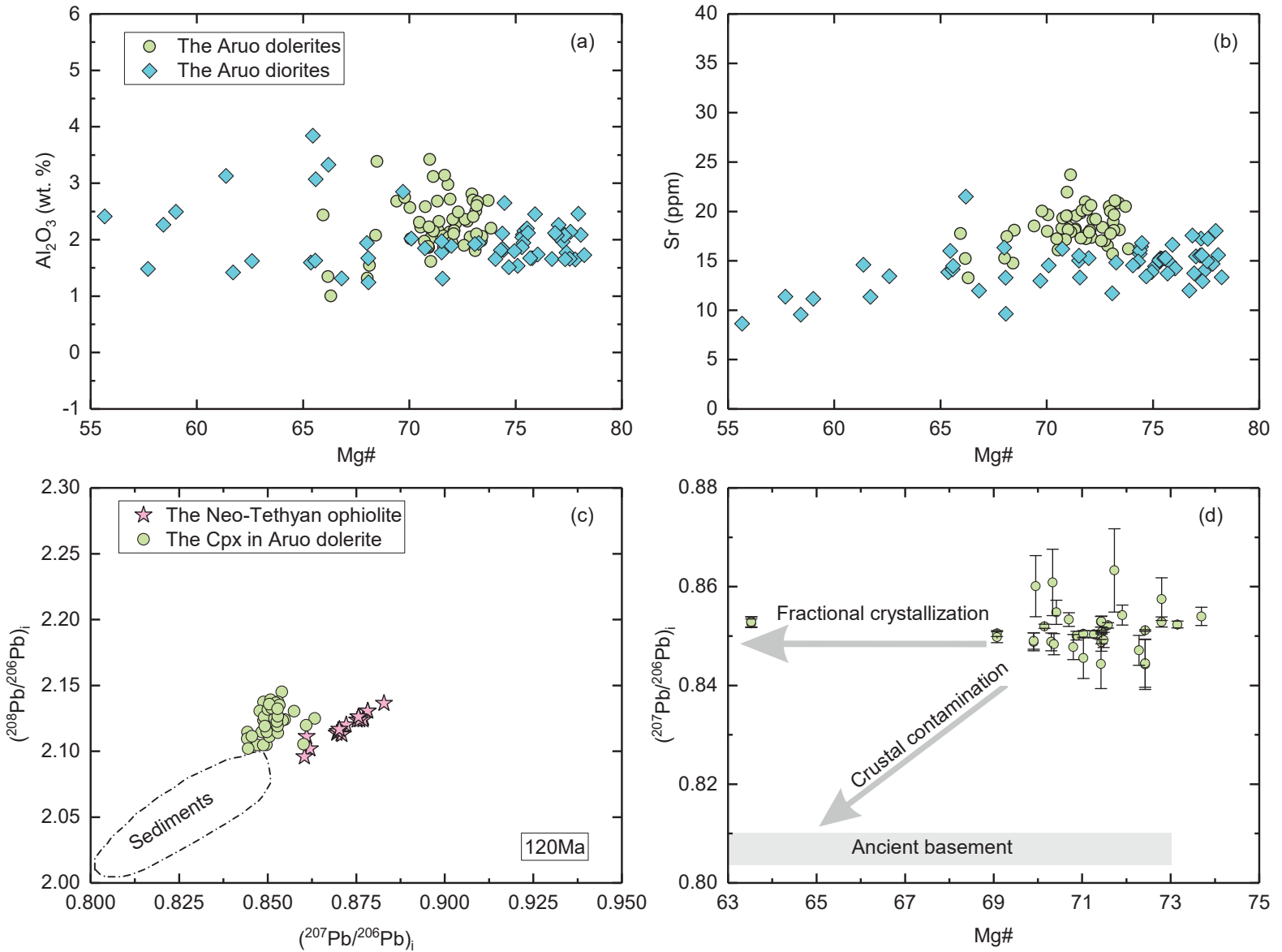


Figure 11

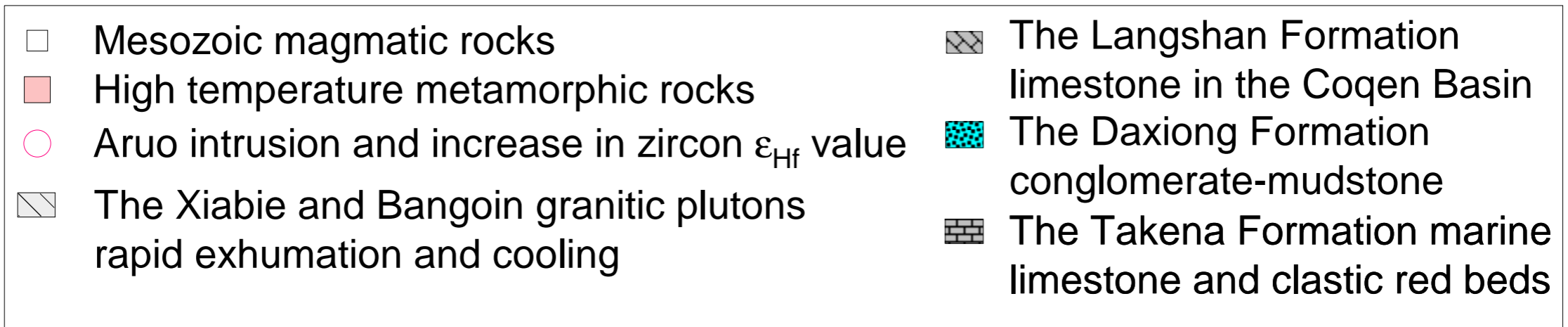
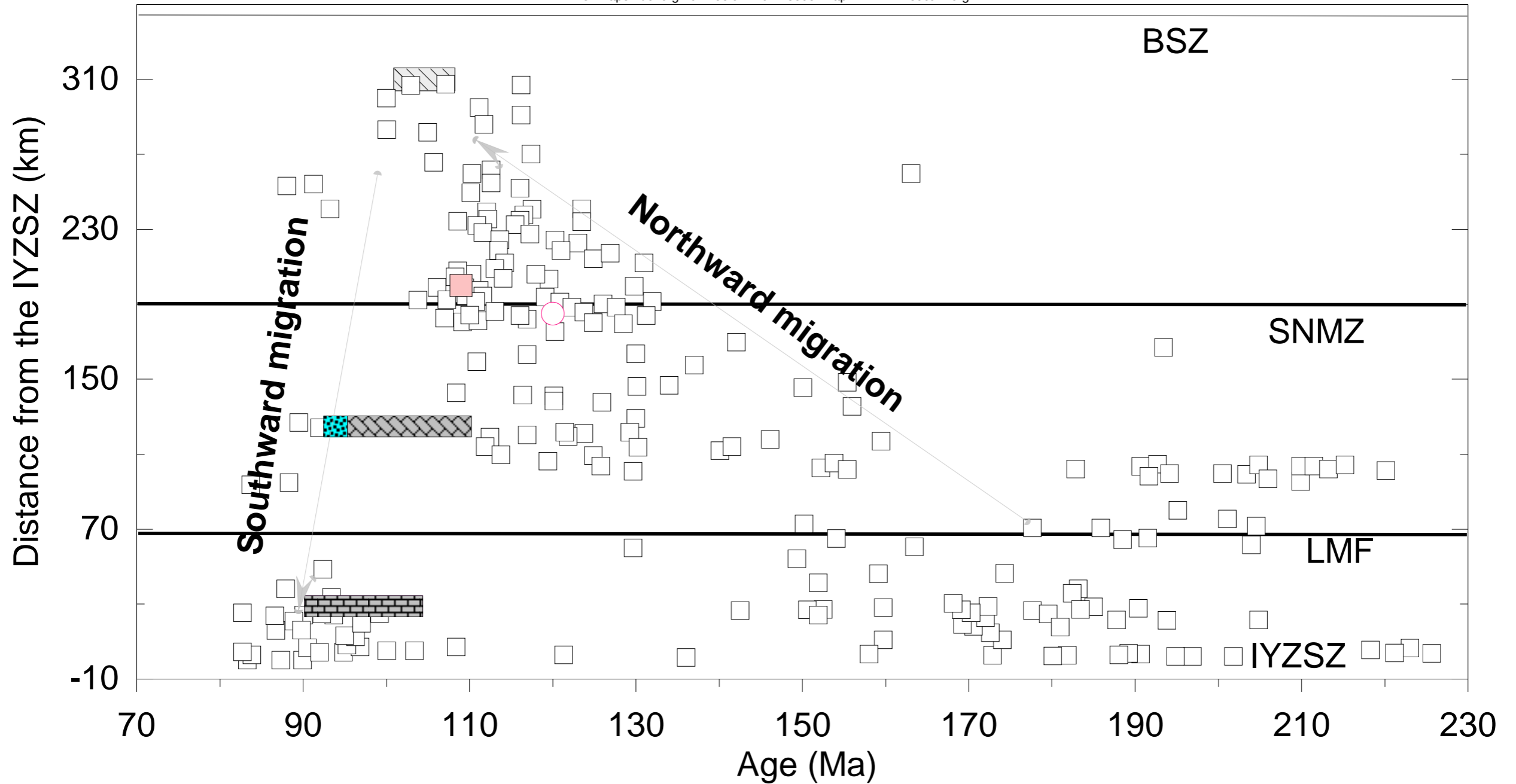


Figure 12

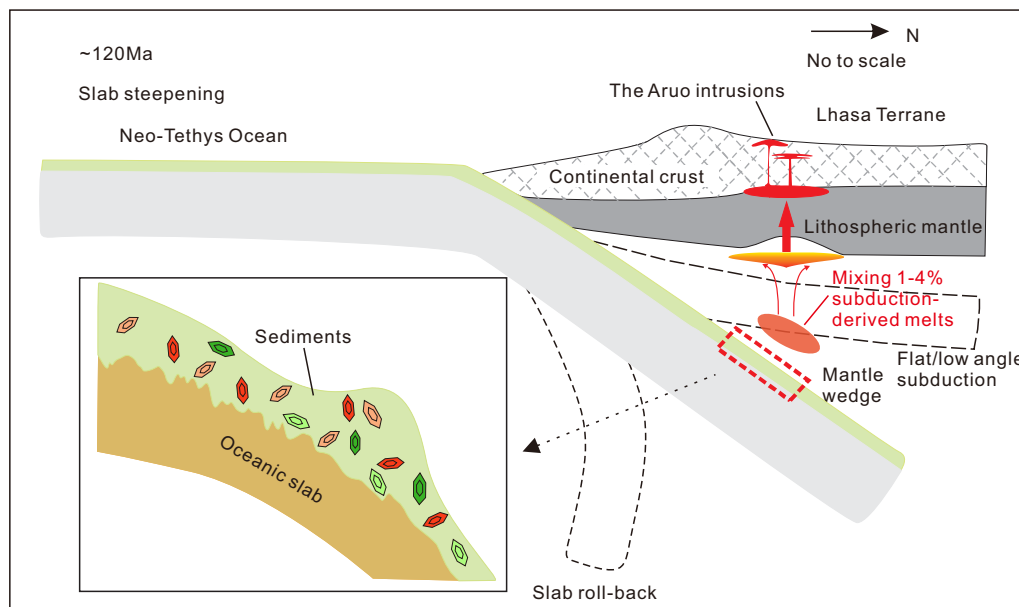


Figure 13